University of Alberta

Increase of collection efficiency in fibrous filter media through magnetic alignment of elongated aerosol particles

by

Christopher O. Lam 

A thesis submitted to the Faculty of Graduate Studies and Research in partial fulfillment of the requirements for the degree of **Master of Science**.

Department of Mechanical Engineering

Edmonton, Alberta
Fall 2008

Your file Votre référence
ISBN: 978-0-494-47287-3
Our file Notre référence
ISBN: 978-0-494-47287-3

Abstract

This research explored the effect of magnetically aligned poly-disperse aerosol fibers on filtration in nylon net filters. Efficiencies of the filters were tested at varying face velocities (1.5, 5.1, and 10.2 cm/sec), magnetite compositions (by mass) (10, 20, and 30%), and magnetic field strengths (0, 50, and $100mT$). Single-fiber theory provided theoretical rationale for fiber behavior in a uniform magnetic field. The filters were challenged with cromoglycic acid coated with magnetite particles. The resulting masses and fiber distributions on the filter and downstream filtrate were measured.

Findings from the experiment, matched by supporting theories, confirmed significant efficiency increases at 1.5 cm/sec at all magnetite compositions, and for 5.12 cm/sec at 20% and 30% compositions. A saturated efficiency was reached for further increases in field strength. The author validates the method and suggests that fiber alignment in a magnetic field could warrant applications in the filtration and fiber detection fields.

Acknowledgements

This completion of this thesis would not be possible without the help of the ARLA lab: Andrew Martin, Biljana Grgic, and Helena Orszanska.

I would like to dedicate this thesis to one individual, G.M. Thank you for giving me the encouragement and motivation to stay on-track.

Table of Contents

List of Figures

Chapter 1

Introduction

The possibility of increasing filter efficiency through the magnetic alignment of high aspect ratio fiber particles, with magnetic nano-particles attached to their surfaces, was explored in this research. The work presented in this thesis required knowledge in three specific areas: The fiber orientation, filtration in a fibrous filter, and the torque exerted on a magnetically susceptible fiber particle in a relatively constant and uniform magnetic field.

The way by which an aerosol particle is captured onto a fibrous filter, in relatively high air-flow, differs from gravitational filtration used in chemistry. Particles much smaller than the pores, created by the fibers of the filter, are captured through the following mechanisms: Sedimentation, Brownian diffusion, inertial impaction, and interception. The first three mechanisms are mainly dependent on the particle's aerodynamic properties, while interception is mainly dependent on the geometric size and shape of the particle. The interception mechanism bears significance for a fiber particle, since the probability of deposition through interception is larger when the particle is aligned with its major axis perpendicular to fluid streamlines as opposed to parallel alignment. The aerodynamic properties also change with particle orientation. However, at low particle Reynolds numbers, the change, in regards to deposition, is not as significant. The second concept mentioned above is the magnetic alignment

of aerosol fibers in motion to increase the likelihood of capture on the filter, through interception.

With the effect of particle orientation on fiber capture in a filter as the underlying concept, an aerosol testing apparatus was created to measure the mass filtration of aerosol fibers in a sampling filter. A uniform magnetic field was placed across the filter, such that the field direction was in plane with the filter. Measurements of the mass efficiency of the filter, with and without the magnetic field, were compared to test the validity of this method.

1.1 Background

The potential health hazards involved with inhalation exposure of asbestos fibers is well known. Even at minute concentrations, extended exposure to asbestos is known to increase the development of mesothelioma, lung cancer, asbestosis, and other lung related illnesses (Bernstein et al. (2001) and V.Timbrell (1982)). Concerns of human health impact stem from the ability of asbestos dust to penetrate deep within the lung. Asgharian et al. (1997), Jeffery (1922) and Chen and Yu (1991) have reported that fibers, entrained in air flow, can assume orientations relative to fluid streamlines, but, have a tendency for parallel alignment of their long axis. High aspect ratio fibers can possess small aerodynamic diameters, attributing to their bypass of the upper airways in the respiratory system. Due to their large geometric size and natural properties, asbestos fibers are not susceptible to the macrophages that remove trapped particles within the lung. Once settled, the deposited fibers can interact with the cells of the pleural lining, which may prove malignant, leading to the aforementioned carcinogenic activity. (Moolgavkar et al. (2001)).

Current building standard codes and regulations have evolved to minimize human health risk to asbestos fibers. Industry compliance to government regu-

lations stipulates the importation, use, disposal and inspection of asbestos and asbestos-containing products in the workplace. Health Canada regulates that occupational health authorities ban friable asbestos fibers and those containing fibrous erionite under the Hazardous Products Act, R.S.C. 1985. Despite policies and monitoring, continued research and prevention is necessary to improve processes in mitigating unwanted passage of harmful fibers to the human body.

Given the characteristics and behavior of fiber deposition in the lung, tremendous opportunities exist in the use of fiber characteristics for the application of therapeutic drug delivery. The ability of drug carrying fibers to penetrate deep into the lung, depositing where the medication is needed, warrant further consideration (Chan and Gonda (1989)). Ulanowski and Kaye (1999) demonstrated the magnetic anisotropy of certain asbestos fibers by alignment in an uniform magnetic field and hypothesized the potential use in asbestos fiber detection. The concept is also of interest for aerosol deposition applications and targeted drug delivery. Martin and Finlay (2008a) and Martin and Finlay (2008b) had recently proven the validity of magnetic alignment of aerosolized cromoglycic acid fibers, with magnetite particles loaded on their surfaces, to increase the deposition in airway models. Cromoglycic acid is used in medical applications for the prophylaxis of asthma (Chan and Gonda (1989)). Magnetite has been well documented for its potential clinical use in targeting drug delivery for cancer therapy (Asmatulu et al. (2004, 2005), Ally et al. (2005)), and also in the hypothermia or heat-shock treatment of cancer (Cheng et al. (2005), and Akira et al. (2003)).

1.2 Fiber Testing and Aerosol Filtration

As noted previously, inhalation of fibers is a contributing factor to the development of various lung diseases. Significant reference literature exists on

the filtration of spherical aerosol particles, however, studies on the filtration of fibers have received less attention.

The motion of a high aspect ratio particle through the air is significantly different from the motion of a spherical particle. The industry standard by which to characterize fibers is by assigning them an equivalent spherical aerodynamic diameter (Harris and Fraser (1976), Gonda and Khalik (1985)). Harris and Fraser (1976), and Gonda and Khalik (1985) derived expressions for the aerodynamic diameter using thin cylindrical rod, and prolate spheroid approximations, respectively, to describe the volume of a single fiber. Also, an entrained fiber can translate and rotate leading to different orientations of its long axis relative to fluid streamlines. Previous authors ensured that all cases were sufficiently considered by proposing different aerodynamic diameters for parallel, perpendicular, and random orientations.

Capture of aerosol particles in fibrous filter media is different than in gravitational analysis used in chemistry. In gravitational analysis, the pore size dictates the particles being filtrated whereas in aerosol filtration, the particle's aerodynamic behavior, flow conditions, and filter media dictates the particles being captured. The filtration efficiency of these non-spherical particles through fibrous filters can be estimated through substitution of their aerodynamic diameters into theoretical filtration expressions for spherical particles. These filtration expressions are from single-fiber efficiency theory and have been used by many authors (Hinds (1982), Baron and Willeke (2001), Lange et al. (1999), Wang et al. (2006), Lee and Liu (1982), and Yeh and Liu (1974)).

Generation of fibrous aerosol with relatively mono-disperse diameters and poly-disperse lengths is possible (Chen et al. (1993)), however, much of the experimental work found described aerosol fibers as poly-disperse in both diameter and length. To the best of the author's knowledge, there has not been a method to generate a mono-disperse fibrous aerosol. One method in analyzing

the concentration and distribution of a poly-disperse aerosol is to implement NIOSH fiber counting procedures to obtain number concentrations. Fiber distributions obtained from upstream and downstream aerosol samples, from a filter medium, can then be compared. The experimental examination of the filtration efficiency of filters, through such methods, has been explored by Su and Cheng (2005), Cheng et al. (2006), and Gentry et al. (1990).

1.3 Objective and Research Direction

The main goal of this research was to investigate the viability of magnetic alignment of fibrous aerosol particles to increase the filtration efficiency of a filter medium. A controlled environment for aerosol testing was created for the purpose of this experiment. The apparatus was built based on the standards for aerosol testing, which has been well documented in aerosol texts (Baron and Willeke (2001) and Vincent (2007)). As part of this research, it was of interest to examine the effect on filtration that varying parameters would yield. It was hypothesized that changes in the parameters below would have an effect on filtration of the fibers.

- Face Velocity (the air velocity immediately upstream from the filter)
- Magnetite content
- Magnetic field strength

Filter efficiencies of particles oriented perpendicular and parallel to fluid streamlines were predicted using single-fiber theory. The efficiency levels were then used as upper and lower limits to compare experimental efficiencies of the fibers with and without the magnetic field, respectively. The single-fiber efficiency predicted for each deposition mechanism provided insight as to which mechanism dominated the deposition. This helped to gain an understanding

of the deposition mechanisms. The results of this experiment are specific to the case of small particle sizes compared to large pore sizes.

Furthermore, the aerosol used in this experiment was poly-disperse and it was of interest to examine the size specific penetration in the aligned and unaligned cases. Size distributions, obtained using fiber counting procedures, were organized by length into size bins and the volume of the particles were calculated using a cylindrical approximation. This data was used to find the size specific penetration.

Finally, the practicality of using this method for the purpose of increasing filter efficiency, possible applications, and future work were addressed.

1.4 Thesis Outline

Chapter 2 provides details on the single-fiber efficiency theory predicting the filtration of a fibrous filter challenged with high aspect ratio particles. Included in this discussion is the characterization of the non-spherical particles with an aerodynamic diameter and their use in the single-fiber theory, previously developed for spherical particles. Following the filtration theory, the fluid dynamic and magnetic torque equations and the assumptions used to arrive at those equations are presented. The discussion of the experimental equipment and procedures are contained in Chapter 3. Details on the sampling filter, aerosol generation, testing apparatus, and analysis procedures are presented first in this chapter. Then, the fiber count methods were utilized to obtain aerosol size distributions and an estimate of the size specific penetration. The results from the experiments and filtration theory, along with a comparison between them, will be provided in Chapter 4. Finally, conclusions from the analysis and future direction will be discussed in Chapter 5.

Chapter 2

Theory

Outlined in Chapter 2 is the filtration theory commonly used in aerosol filtration. Section 2.1 describes the method to characterize the fibrous particles using an equivalent aerodynamic diameter of a sphere. The theory's significance lies in its ability to provide a means to predict how a fiber particle behaves in shear flow, and it was necessary since much of the filtration theory available was developed for spherical particles. The modes of particle deposition and their single-fiber efficiencies for spherical particles are discussed in section 2.2 and also extended to high aspect ratio particles. For fibers, the most significant deposition mechanism is interception, since the probability of capturing a fiber perpendicular to the flow is significantly lower than a fiber parallel to the flow. In order to predict whether fibers will align due to an external magnetic field, Section 2.3 compares the magnetic torque (Martin and Finlay (2008a)) and the aerodynamic torque on the fiber particle.

2.1 Sedimentation and Inertial Impaction Aerodynamic Diameters

An approach to predicting the motion of entrained fibers was to use the equivalent aerodynamic diameter of fibers. This method assigned a different

aerodynamic diameter for the parallel, perpendicular, and random orientations that a fiber particle can maintain during its time airborne. The fluid resistance was important in determining the aerodynamic effect due to gravity, inertia, and diffusion (Harris and Fraser (1976) and Balashazy et al. (1990)). Therefore the basis by which sedimentation and inertial impaction aerodynamic diameters were estimated was through viscous drag on a fibrous particle, F_d. Assuming $Re << 1$, Stokes Law, Equation 2.1, applies.

$$F_d = 3\pi\mu U_o d_{eq} \tag{2.1}$$

where μ is the fluid viscosity (in our case air) and d_{eq} is the diameter of a sphere with the equivalent viscous drag as the prolate spheroid or fiber (Harris and Fraser (1976)). An expression for the diameter of the equivalent sphere for a fiber with its long axis parallel to the direction of flow is given by Equation 2.2.

$$d_{\parallel} = \frac{2d_f\beta}{3\left(\ln(2\beta) - 1/2\right)} \tag{2.2}$$

Here, d_f is the diameter of the fiber, and β is the ratio of the fiber length to diameter. An expression for the diameter of the equivalent sphere for a fiber with its long axis normal to the direction of flow is given by Equation 2.3.

$$d_{\perp} = \frac{4d_f\beta}{3\left(\ln(2\beta) + 1/2\right)} \tag{2.3}$$

The viscous drag is equivalent to the force of gravity when the particle has reached terminal or settling velocity (Equation 2.4). Harris and Fraser (1976) approximated the volume of the fiber with that of a thin straight cylinder, with diameter, d_f, and length, l_f ($V = \pi d_f^2 l_f$).

$$U_{s,f} = \frac{d_f^2\rho g\left[\ln(2\beta) - 1/2\right]}{16\mu} \tag{2.4}$$

To obtain the equivalent aerodynamic diameter, the settling velocity for a fiber, of density, ρ, given in Equation 2.4 is equated to the settling velocity

of a spherical particle. Considering first a high aspect ratio particle traveling with its long axis parallel to the motion, the resulting expression for the sedimentation, diffusion, and inertial impaction aerodynamic diameters is given by Equation 2.5 (Harris and Fraser (1976)).

$$d_{ae\parallel} = \frac{3}{2} d_f \sqrt{\frac{\rho}{\rho_o}[\ln 2\beta - 0.5]} \tag{2.5}$$

Similarly, the aerodynamic diameter of a high aspect ratio particle with its long axis perpendicular to the motion is given in Equation 2.6 (Harris and Fraser (1976)).

$$d_{ae_\perp} = \frac{3}{4} d_f \sqrt{\frac{2\rho}{\rho_o}[\ln 2\beta + 0.5]} \tag{2.6}$$

Subsequent analysis will indicate a significant difference in aerodynamic properties of a fiber in different orientations. The aerodynamic diameters were calculated based on the count median dimensions of the aerosol fibers (Section 3.7). Using these expressions and the single-fiber theory presented in the next section, an estimate of the filtration efficiency of a fibrous filter was made possible.

2.2 Filtration Theory

The single-fiber filtration efficiency of the fibrous filters challenged with aerosol (Hinds (1982) and Baron and Willeke (2001)) was modified for nylon net filters (Yamamoto et al. (2005)). Single-fiber theory stipulates that the fluid streamlines around a fiber are not distorted significantly by surrounding filter fibers. A staggered array of cylinders model was used to approximate the structure of the filter and the velocity flow field was solved for analytically (Hinds (1982)). Expressions to predict the probability of particle capture by the single fiber were solved from particle equations of motion and the surrounding flow field. The single-fiber efficiencies were then extrapolated

to give the overall efficiency of the bulk filter. The overall efficiency of the aerosol particles was defined as the ratio of amount of particles deposited on the filter over the total amount of particles incident on the filter material. The relationship between the overall penetration, **P**, and overall efficiency, **E**, is given by Equation 2.7.

$$\mathbf{P} = 1 - \mathbf{E} \tag{2.7}$$

The volume fraction of the fibers to total volume of the filter is denoted by α.

$$\alpha = \frac{\text{volume of fibers}}{\text{volume of filter}} \tag{2.8}$$

Before presenting the deposition mechanisms, it is important to distinguish the flow velocity inside the filter material from the more commonly reported parameter, the face velocity. The face velocity, U_o is inversely proportional to the flow velocity inside the filter, U, by the factor $1 - \alpha$. In the single-fiber expressions U_o is used rather than U.

$$U = \frac{U_o}{1 - \alpha} \tag{2.9}$$

As aerosol travels past the fibers of a filter, particles can deposit on fiber surfaces through the following important mechanical processes:

- Gravitational Deposition, E_{grav}
- Brownian Diffusion, E_{diff}
- Impaction, E_{imp}
- Interception, E_{int}

Single-fiber theory normally calculates the contributions to deposition on a single fiber through the above mechanisms, however, the nylon net filter possessed a very regular pattern and therefore the theory was modified. The deposition from interception was predicted using a hole model approximation

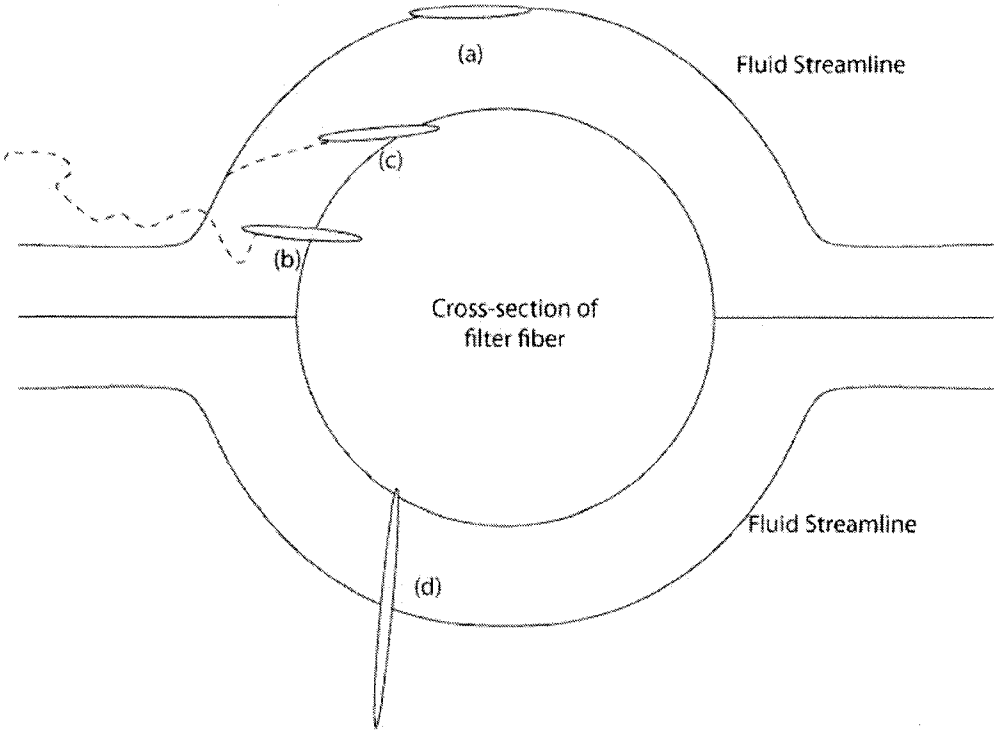

Figure 2.1: Fiber behavior: (a) A penetrating fiber. (b) A fiber depositing through diffusion. (c) A fiber depositing through inertial impaction. (d) A fiber depositing through interception.

while the regular single-fiber theory was used for inertial impaction, gravitation, and diffusion (Yamamoto et al. (2005)). As a first approximation, the arithmetic sum of the contributions from the deposition processes is used to predict **E**, but the different deposition mechanisms are competing for the same particles. Therefore, a more appropriate estimate would be from Equation 2.10 (Yamamoto et al. (2005)).

$$\mathbf{E} = 1 - (1 - E_{grav})(1 - E_{diff})(1 - E_{imp})(1 - E_{int}) \tag{2.10}$$

Here, E_{grav}, E_{diff}, and E_{imp} are the overall capture efficiencies by the respective mechanical process. They are calculated by multiplying the single-fiber efficiencies by the projected volume fraction of fibers in the filter. E_{int} represents the overall capture efficiency of interception as calculated through the square hole model (Yamamoto et al. (2005)). Descriptions of the deposition mechanism as well as the equations for the corresponding single-fiber efficiencies follow in Sections 2.2.1 to 2.2.4. The single-fiber efficiency equations from Hinds (1982) and Baron and Willeke (2001) are summarized below in equations 2.11 to 2.21.

2.2.1 Gravitational Deposition

A particle will settle in a fluid under the force of gravity. The "terminal velocity" or "settling velocity" determines the rate at which the particle descends in the fluid. The effect of gravity is important in the deposition of particles, as a sufficiently large settling velocity can cause a particle to deviate from fluid streamlines and collide with nearby surfaces. Gravitational deposition is important when fluid velocity is low and particle size is large.

The single-fiber efficiency for deposition by gravitational settling is given in Equation 2.13 and the ratio of the settling velocity of the aerosol particle, $U_{s,f}$, to the fluid flow velocity just upstream of the single fiber, U, is given

in Equation 2.11. $U_{s,f}$ of the aerosol particle with an aerodynamic diameter, $d_{ae,p}$, is given by Equation 2.4.

$$G = \frac{U_{s,f}}{U_o} = \frac{\rho_p d_{ae,p}^2 C_c g}{18 \mu U_o} \tag{2.11}$$

ρ_p is the density of the aerosol particle, μ is the viscosity of the surrounding fluid, and C_c is the Cunningham slip factor given in Equation 2.12.

$$C_c = 1 + \frac{\lambda}{d_{ae}} \left[2.34 + 1.05 exp\left(-0.39 \frac{d_{ae}}{\lambda} \right) \right] \tag{2.12}$$

λ here is the mean free path of air, $0.067 \mu m$.The overall efficiency for this deposition mechanism is given by Equation 2.13.

$$E_{grav} \simeq (1 - \epsilon)\, G\, (1 + R) \tag{2.13}$$

ϵ is the percentage of open area through the filter. $(1 - \epsilon)$ represents the projected fraction of fibers and is multiplied by the single-fiber efficiency of gravity to give the overall filtration. To arrive at the sedimentation single-fiber efficiencies of fiber particles in parallel and perpendicular, $d_{ae,p}$ in Equation 2.11 is substituted with $d_{es_\parallel}$ (Equation 2.5) and $d_{es_\perp}$ (Equation 2.6), respectively.

2.2.2 Deposition by Brownian Diffusion

Brownian motion, which affects very small particles, is the result of particle collisions with the molecules in the surrounding fluid, causing the particle to travel in a random trajectory different from fluid streamlines. Diffusion plays an important role in the filtration of particles, since smaller particles have a tendency to move away from streamlines, depositing on the surface of a single fiber in the filter. Figure 2.1(b) illustrates this deposition mechanism.

The Peclet number, Pe, given by Equation 2.14, is the non-dimensional parameter governing the single-fiber efficiency for this mechanism (Equation 2.15). Pe is defined as the ratio of the single fiber diameter multiplied by the

upstream fluid velocity, U_o, over the particle diffusion coefficient, D_p given in Equation 2.16.

$$Pe = \frac{d_{ae,p} U_o}{D_p} \tag{2.14}$$

$$E_{diff} = (1-\epsilon)\, 2.58 \left(\frac{1-\alpha}{Ku}\right)^{1/3} Pe^{-2/3} \tag{2.15}$$

$$D_p = \frac{kTC_c}{3\pi\mu d_{ae,p}} \tag{2.16}$$

In Equation 2.16, $k = 1.38 \times 10^{-2/3} \frac{J}{K^3}$ is Boltzmann's constant, T is the temperature in Kelvin, and C_c is given above in Equation 2.12. The diffusion single-fiber efficiencies of fiber particles were found by substitution of $d_{ae,p}$ in Equation 2.14 with $d_{es_\parallel}$ (Equation 2.5) and $d_{es_\perp}$ (Equation 2.6).

2.2.3 Deposition by Inertial Impaction

Deposition by impaction occurs when a particle with sufficient inertia overcomes the fluid shear forces which align the particles, causing the particle's trajectory to stray away from streamlines and collide with nearby surfaces. Figure 2.1(c) illustrates this deposition mechanism. Deposition by inertial impaction increases with increasing flow velocities and greater particle mass.

The importance of particle inertia is estimated using the Stokes number, denoted by Stk. The single-fiber efficiency is given by Equation 2.19 and varies proportionally with Stk.

$$Stk = \frac{\tau U_o}{D_f} = \frac{\rho_p d_{ae,p}^2 C_c U_o}{18\mu D_f} \tag{2.17}$$

$$J = \left(29.6 - 28\alpha^{0.62}\right) R^2 - 27.5 R^{2.8} \quad \text{for } R < 0.4 \tag{2.18}$$

$$E_{imp} = (1-\epsilon)\frac{J\,(Stk)}{2Ku^2} \tag{2.19}$$

Here, the relaxation time is denoted by τ and the Cunningham slip factor by C_c given by Equation 2.12. An examination of Equations 2.17 and 2.19 shows

that an increase in particle inertia ($\uparrow d_{ae,p}$ or $\uparrow \rho_p$) or a more abrupt change in curvature of the fluid streamlines ($\downarrow D_f$) results in a greater probability of deposition. To find the inertial impaction, single-fiber efficiences of fiber particles in parallel and perpendicular, $d_{ae,p}$ in Equation 2.19 were found by substitution of $d_{ei_\parallel}$ (Equation 2.5) and $d_{ei_\perp}$ (Equation 2.6), respectively.

2.2.4 Deposition by Interception

Interception is not a result of a particle traveling on a different path from fluid streamlines as in sedimentation, Brownian diffusion, and inertial impaction. Interception occurs when a particle, traveling along a streamline, comes sufficiently close into contact with a surface due to its geometry. Figure 2.1(d) illustrates this deposition mechanism. Interception is important for high aspect ratio particles because the probability of deposition depends on particle orientation. Figure 2.1(a) and (d) depict two fiber particles flowing past a single fiber of the filter. Both particles traveled with their centers of gravity along streamlines, but the lower particle was captured due to its perpendicular orientation, whereas the upper particle passed without depositing. The probability of interception is much lower when the fiber particle is aligned parallel to the flow compared to when it is aligned perpendicular to the flow.

Consideration was first given for the case of a spherical particle with diameter. The calculation of E_{int} was made using the square hole model and assuming a uniform velocity profile within the hole. The model considers a particle captured if its center travels within a distance such that the particle comes into contact with a fiber of the filter. By assuming a uniform velocity profile the fraction of spherical particles captured is the area ratio of a square with side length $l-d$ to the square hole of side length l, where d is the spherical particle diameter and l is the pore dimension. The same probability of interception was used for unaligned fibers in the present study. The deposition by

interception for a fiber particle, however, differs depending on orientation and the fraction of aligned fibers captured is the area ratio of the rectangle of side lengths $l - l_f$ and $l - d_f$ to the area of the square hole. l_f and d_f are the length and diameter of the fiber particle. The expression for the overall efficiency due

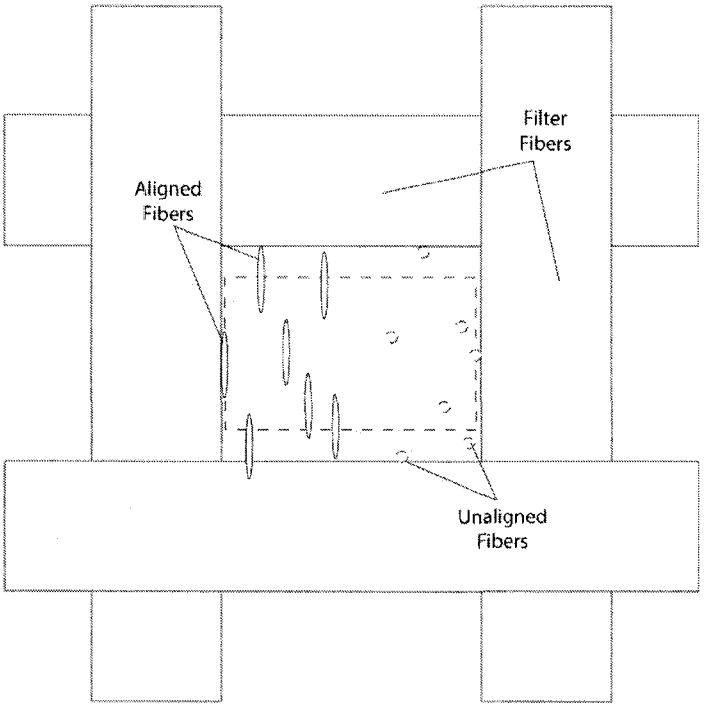

Figure 2.2: Deposition through interception in a rectangular hole model. The dotted rectangle represented the aligned fibers that penetrated the filter.

to interception for unaligned and aligned fibers is given by Equation 2.20 and Equation 2.21.

$$E_{int} = 1 - \left(\frac{l - d_f}{l}\right)^2 \tag{2.20}$$

$$E_{int} = 1 - \left(\frac{l - l_f}{l}\right)^2 \tag{2.21}$$

2.3 Aerodynamic and Magnetic Torque

As previously mentioned, aerosol fibers traveling in a fluid flow will undergo tumbling and rotations, though for aspect ratios above 5, particles experience preferential alignment with streamlines. In order to align fibers as to increase the probability of deposition by interception, the aerodynamic torque exerted on the fiber by the surrounding fluid must be overcome. The proposed mechanism to achieve this involved applying a constant magnetic field across the surface of the filter to align the fibers, with a magnetic nano-particle coating, as shown in Figure 2.3. Martin and Finlay (2008a) showed that fibers

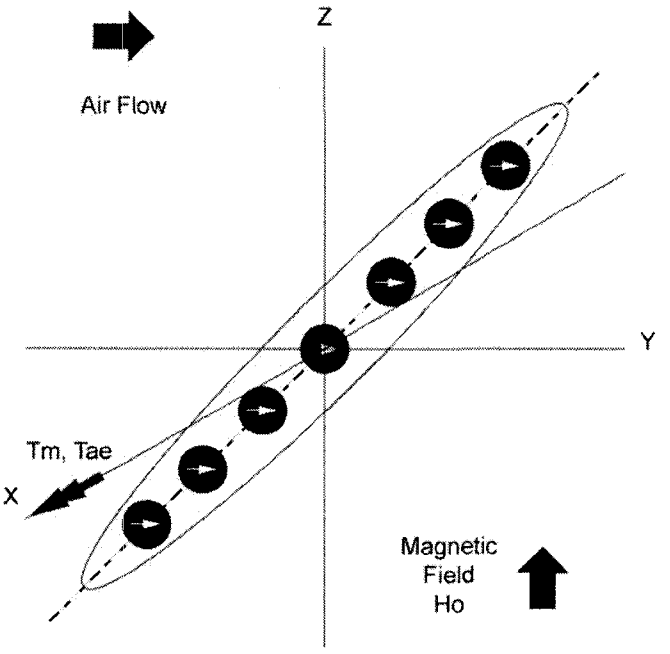

Figure 2.3: A fiber particle entrained in air flow and under the influence of an applied uniform magnetic field. The aerodynamic torque, $\vec{T}_{ae}$, and magnetic torque, $\vec{T}_m$, are shown acting on the x-axis perpendicular to the x-z plane.

without magnetic properties could be coated with magnetic nano-particles

and exhibit magnetic susceptibility. The fibers aligned in the presence of a uniform magnetic field and the flow conditions of small airway models. In order to determine the feasibility of aligning fibers by introducing a magnetic field, a comparison of aerodynamic and magnetic torque on the fiber particle with magnetic material distributed along its surface was done based on the equations presented in the aforementioned work.

2.3.1 Aerodynamic Torque

Aerosol fibers were treated as particles with an ellipsoidal shape, and the aerodynamic torque from the motion of the surrounding fluid were predicted from equations developed by Jeffery (1922). Considering the case of simple linear shear flow in Figure 2.3, the aerodynamic torque, $T_{ae,x}$, acting on the particle was estimated by Equation 2.22 (Martin and Finlay (2008a)).

$$T_{ae,x} = \frac{2\pi\mu G d_f^2 l_f \left(d_f^2 \cos^2\theta + l_f^2 \sin^2\theta\right)}{3\left(d_f^2\beta_o + l_f^2\gamma_o\right)} \tag{2.22}$$

Here, μ is the fluid viscosity, d_f and l_f, respectively, are the fiber particle's diameter and length, θ is the angle the fiber makes with the velocity direction, and G is the velocity gradient. β_o and γ_o were given by Gallily and Cohen (1979), and are shown in Equation 2.23 and Equation 2.24

$$\beta_o = \frac{\beta^2}{\beta^2-1} + \frac{\beta}{2\left(\beta^2-1\right)^{3/2}} \ln\left[\frac{\beta - \sqrt{\beta^2-1}}{\beta + \sqrt{\beta^2-1}}\right] \tag{2.23}$$

$$\gamma_o = \frac{-2}{\beta^2-1} - \frac{\beta}{\left(\beta^2-1\right)^{3/2}} \ln\left[\frac{\beta - \sqrt{\beta^2-1}}{\beta + \sqrt{\beta^2-1}}\right] \tag{2.24}$$

2.3.2 Magnetic Torque of Fibers in a Constant Magnetic Field

Shine and Armstrong (1987) predicted the motion of a ferromagnetic axis-symmetric ellipsoid suspended in a stationary fluid and under the influence

of a magnetic field. The uniform field induced the magnetic torque, $\vec{T_m}$, experienced by the ferromagnetic axis-symmetric ellipsoid is given as Equation 2.25.

$$T_m = \mu_o \int_V \left(\vec{M}_p \times \vec{H}_o \right) dV \tag{2.25}$$

Ferromagnetic materials and certain types of asbestos fibers exhibited magnetic anisotropy which was suggested as one of the key contributors to the alignment of fibers (Ulanowski and Kaye (1999)). In Equation 2.25, μ_o is the permeability of free space, $\vec{M}_p$ is the magnetization at any point on the particle and a property of the material itself, and $\vec{H}_o$ is the external magnetic field strength. For a ferromagnetic material, $\vec{M}_p$ is related to the internal magnetic field, $\vec{H}_i$, and reaches a saturation magnetism at large $\vec{H}_o$. $\vec{M}_p$ and $\vec{H}_i$ also vary within the body depending on the particle shape. However, $\vec{M}_p$ for the nonpermanent ferromagnetic ellipsoid above could not be used for the present case of an inhomogeneous composite fiber particle. Martin and Finlay (2008a) have instead treated the magnetite particles as ideal dipoles, calculated the resulting magnetic field for two neighboring dipoles, and approximated $\vec{M}_p$ as the contributions of the dipole fields to the internal magnetic field. With this interpretation of magnetization, the magnitude of the magnetic torque on a single fiber particle, with magnetite material distributed along its surface, is:

$$T_m = 2\mu_o V_f H_o M \left(\frac{d_d}{L} \right)^2 \sin\phi \cos\phi \tag{2.26}$$

where M and H_o are the magnitudes of the $\vec{M}_p$ and $\vec{H}_o$, respectively, $\frac{d_d}{L}$ is the ratio of the diameter of the deposit to the spacing between dipoles, V_f is the volume of the fiber particle, and ϕ is the angle the fiber's major axis makes with the direction of $\vec{H}_o$ (Figure 2.3).

Equations 2.22 and 2.26 were used to compare the aerodynamic torque and magnetic torque on the fiber for various velocity gradient, fiber particle sizes, and magnetite loadings.

2.3.3 Force on Fibers in a Magnetic Field

The approximation of a uniform and constant magnetic field ($\nabla H_o = 0$) was used in the analysis of the magnetic torque on a fiber particle. In actuality, the magnetic field varied across the surface of the filter. To test the significance of this gradient in the magnetic field, $H_{o,gradient}$, estimations of the magnetic force on the particle, and the distance that the particle would travel due to this force, were made. Similar to the estimation of the magnetic torque on the particle, the magnetite particles are treated as ideal dipoles which align to the external magnetic field, $\vec{H}_o$, shown in Figure 2.4. The magnetic field around a

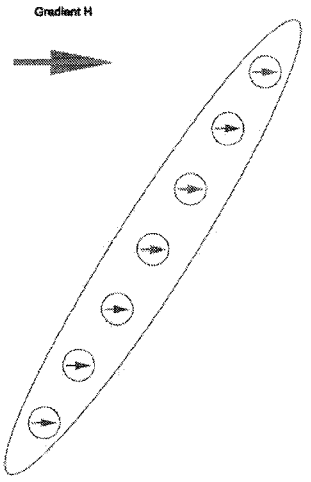

Figure 2.4: The magnetic force on a fiber with magnetite deposits on its surface. The magnetite particles were treated as ideal dipoles

single magnetite particle will be subjected to the influences of the surrounding magnetite particles. Since only an order of magnitude estimate was needed to determine the significance of this force, the effects of neighboring particles were disregarded. The magnetite particles were treated as ideal dipoles, with the magnetic force on each dipole calculated. The total magnetic force, F_m, was then calculated as the summation of the force on each magnetite particle

(Equation 2.27 and Equation 2.28).

$$\vec{F}_m = \mu_o \int_{V_1} \left(\vec{M}_p \cdot \nabla \vec{H}_o\right) dV_1 + \mu_o \int_{V_2} \left(\vec{M}_p \cdot \nabla \vec{H}_o\right) dV_2 + \mu_o \int_{V_3} \left(\vec{M}_p \cdot \nabla \vec{H}_o\right) dV_3 + \cdots \tag{2.27}$$

$$\vec{F_m} = \mu_o \vec{M}_p \nabla \vec{H}_o \left[V_{m,1} + V_{m,2} + V_{m,3} + \cdots\right] = \mu_o M H_{o,grad} V_{p,m} \tag{2.28}$$

$$F_m = \mu_o M H_{o,grad} \left[\chi_{frac} \frac{\pi}{4} \left(d_f\right)^2 \left(l_f\right)\right] \tag{2.29}$$

The bulk volume fraction of magnetite to cromoglycic acid, χ_{frac}, was used here and the volume of the particle was approximated as a cylinder. The length and diameter (l_f and d_f) were determined by the size distribution of the aerosol particles, which was found experimentally.

Chapter 3

Methodology

Chapter 2 presented theories on the aerodynamic behavior of a fiber particle, deposition mechanisms, filter efficiencies of fibrous filters, magnetic and aerodynamic torque. Chapter 3 presents the procedural method to determine the experimental differences in overall efficiency of a filter challenged with fibers, exhibiting magnetic properties, with and without a constant magnetic field in place. Nylon net filters were chosen as the testing filter media for its regular pore shape and variable size. The fibrous aerosol was created through the nebulization of cromoglycic acid and magnetite particles in suspension, discussed in Section 3.2. An experimental testing apparatus and procedure for the testing of efficiency of filters was designed based on the established methods given in Baron and Willeke (2001) and Vincent (2007). The method used to measure the masses of cromoglycic acid fibers collected on the filter and downstream of the filter was UV mass spectrometry. From the mass data, the overall fiber penetration through the filter was calculated. Fiber counting procedures from NIOSH 7400 were employed to obtain an overall upstream and downstream aerosol particle concentration as well as a size distribution of the challenge aerosol. The size-specific penetration of the fibers through the filter was calculated from the particle count data.

3.1 Nylon Net Filters

The filters chosen for the experiment were Millipore™ nylon net filters. Figure 3.1 is an image of the filter taken with a scanning electron microscope. Preliminary evaluations deemed most commercially available filters as

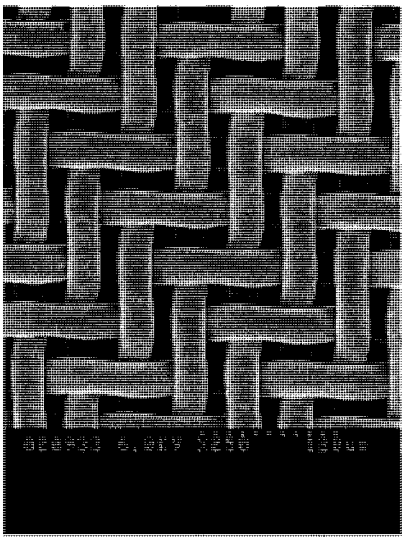

Figure 3.1: Nylon Net Filters

too efficient, inconsistent in pore sizes, or were difficult to examine through UV assaying. High efficiency filters captured most of the aerosol fibers and required very long run times in order for a detectable amount of cromoglycic acid fibers to be captured downstream. The nylon net filters are normally used for particle analysis, gravimetric analysis, and background particulate capture but have not been used in aerosol testing to the knowledge of the author. The net filter was chosen because of its consistent pattern of woven fibers, compatibility with NaOH solvent, ease of examination through assay, and the variety of filtering efficiencies available, dictated by their mesh openings (10 - 180 μm). The nylon net filters possessed a diameter of 47 mm and mesh

openings of 20 μm. The mesh opening, ϵ, was 14% and the packing density, α, was 0.55 (Yamamoto et al. (2005)).

3.2 Preparation of Aerosol Fibers

Aerosol fibers were prepared from cromoglycic acid precipitate and magnetite particles, both of which have been studied and recognized for their medical applications (Chan and Gonda (1989), Akira et al. (2003)). Cromoglycic acid, a drug used in the treatment of the prophylaxis of asthma, can be engineered to form elongated particles (Chan and Gonda (1989)). Magnetite nano-particles with diameters in the nanometer scale were produced using the method of creating a dispersion of Fe_3O_4 nanoparticles in aqueous solution from Cheng et al. (2005). The method of generating the composite fibrous aerosol particles was given by Martin and Finlay (2008b). 15 mg of cromoglycic acid precipitate was measured using a digital balance and placed into a vile. The desired amount of magnetite was withdrawn from a suspension of magnetite particles (concentration = 22.5 $\mu g/mL$) and diluted to 3 mL with distilled H_2O. Once diluted to 3 mL, the magnetite suspension was put into a vile and sonicated for 35 minutes to break apart clusters of magnetite particles. The magnetite suspension was pipetted into the vile of cromoglycic acid and pipetted 50 times. The combined suspension was put on a pressure activated shaker ensuring complete breakdown of clumps of magnetite particles and cromoglycic acid fibers.

3.3 Fiber Testing

The nylon net filters were tested in this experiment based on the standard techniques of aerosol testing. The objective of the experiment focused on changes in capture efficiency with varying face velocity, magnetite composition,

and magnetic field strength. The testing apparatus and procedure is explained below.

3.3.1 Testing Procedure

The filtration efficiency of the nylon net filter was tested using the experimental setup as shown in Figure 3.2. Following the preparation of the aerosol fibers, the suspension was placed into the chamber of the jet nebulizer chamber at position [A] in the experimental setup.

Aerosol fibers unable to navigate through the pores of the nylon net filter were captured and those able to were caught downstream on a Respirgard™ [I], a high efficiency filter manufactured by Vital Signs, Inc. The amounts of cromoglycic acid fibers captured on the nylon net filter and the Respirgard™ were measured using a UV mass assay, which will be discussed in Section 3.5.1. The vacuum pump at position [M] of the test apparatus provided the pressure differential, allowing for the movement of aerosol through the line, and the flow rate was adjusted to the desired values using the needle valve at [L]. While the nebulizer compressor and vacuum pump were switched on, the time required for the aerosol to travel from the nozzle of the nebulizer to the filter holder was not included. To ensure that the runtime, t_r, recorded was a measure of the time between when the filter was first exposed to the aerosol to the end of the experiment, the three way valve at position [K] was set to divert flow into the blank line for one minute before switching flow to the main line. One minute was more than sufficient for the fibrous aerosol to reach the junction at [D] and decrease the time required for the aerosol to reach the filter.

Polydisperse water droplets, containing the cromoglycic acid fibers, were aerosolized using the LC star nebulizer [A] powered by a compressor pump. The aerosol was conditioned by having first passed through two dessicant air drying towers [B] and then through the charge neutralizer at [C] before reach-

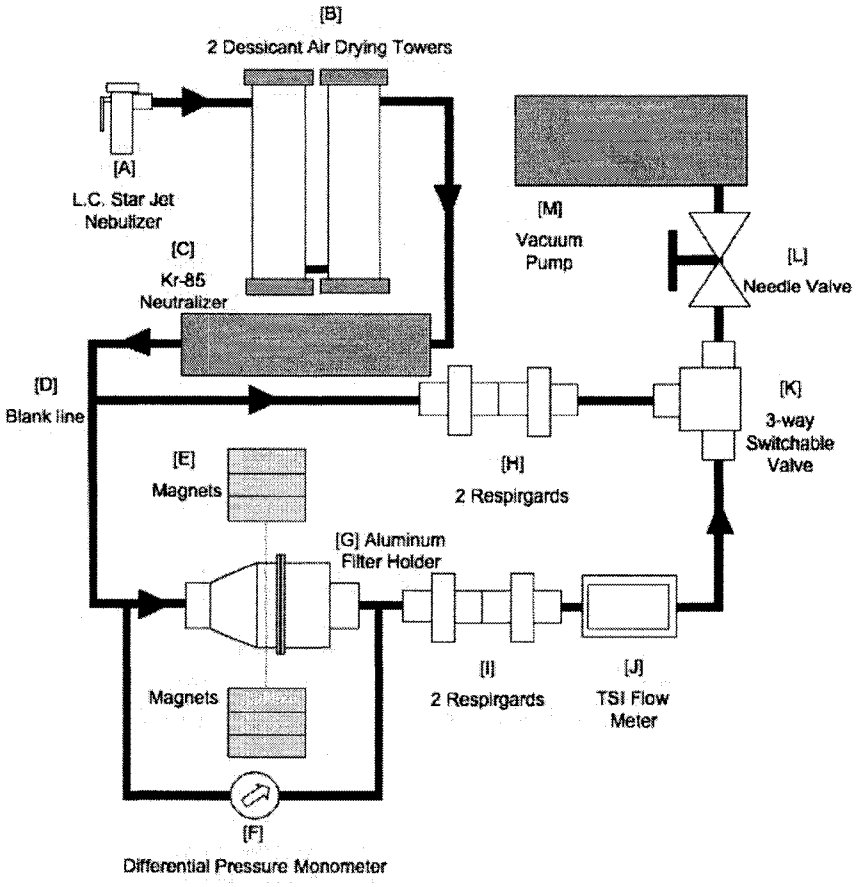

Figure 3.2: Experimental apparatus to test the efficiency of the nylon net filter challenged with cromoglycic acid fibers coated with magnetite particles. The nylon net filter is contained within the aluminum filter holder at [G]. To compare the effect of a constant magnetic field, the experiments are run with the magnets at [E] and again without.

ing the filter. The water droplets were drawn from the nebulizer nozzle and into the two dessicant air drying towers, which aided in the evaporation of the water so that only the fibrous aerosol remained. The drying chamber of each dessicant tower was composed of a netted annular tube surrounded by silica gel, which naturally attracts moisture away from liquids and gases. Confirma-

tion that the water in the aerosol, traveling at flow rates of up to 7 L/min, was completely removed using the two dessicant air dryers, rated to effectively remove absorb moisture at 4 L/min, was explored. An investigation using a humidity meter determined that even at flow rates up to 15 L/min, the humidity level downstream from the drying towers decreased significantly indicating that water was removed, leaving just the aerosol fiber particles.

Consideration was given to the capture efficiency of electrostatically charged aerosol particles (Finlay (2001), Vincent (2007), Baron and Willeke (2001)). To address this, a Kr-85 charge neutralizer was installed at position [C] to neutralize the electrostatic charges on the aerosol particle before the particles reached the filter holder.

The nylon net filter was placed inside the filter holder at [G] between two teflon rings, and a perforated aluminum sheet supported the filter from the downstream side such that the face of the filter was perpendicular to the flow at all times. Pressure drop across the filter was monitored using an Omega HHP-103 pressure manometer attached to two pressure taps placed in the filter holder at locations of equal cross-sectional area, upstream and downstream of the filter. A change in the pressure difference across the filter provided a means to monitor filter loading by aerosol particles. Readings on the monometer were recorded at 30 second intervals beginning with the initial pressure when the filter was first exposed to the aerosol and ending with the final pressure at the end of the experiment. The Respirgard™ attached downstream of the filter acted as an absolute filter to catch the particles that penetrated the nylon net filter. The second Respirgard™ filter at [I] and the two Respirgard™ filters at [H] were installed as a precaution to prevent damage to the vacuum pump and flow meter.

It was necessary to maintain a constant air flow rate for the duration of the sampling run, but changes in pressure difference across the filter from

particle loading could affect the value in the line (Vincent (2007)). The three-way valve had the added effect of presenting a sufficiently high resistance to pressure downstream of the testing filter and upstream from the vacuum pump. The pressure drop across the valve effectively masked any contribution to the total pressure in the sampling line from filter loading and served as a means to control the flow rate through the line. The flow rate was also monitored and recorded at 30 second intervals beginning with the initial flow rate to the final flow rate. Experimental runs were performed with and without the

Table 3.1: The face velocity, magnet spacing, and the percent of magnetite by weight for each sampling run

Experiment	Face Velocity $[cm/sec]$	Magnet Field Strength $[mT]$	Magnetite [% by weight]
1	1.46	100	10
2	1.46	100	20
3	1.46	100	30
4	5.12	100	10
5	5.12	100	20
6	5.12	100	30
7	10.23	100	10
8	10.23	100	20
9	10.23	100	30
10	1.46	50	10
11	1.46	50	20
12	1.46	50	30
13	5.12	50	20
14	5.12	50	30

magnetic field (Section 3.4) at position [E] and the corresponding efficiencies were compared. The independent variables in question were the face velocity, magnetic field strength, and the percent composition of magnetite particles summarized in Table 3.1. U_o introduced in Section 2.2 was calculated from the known area of the filter holder and measured flow rate. The face velocity

was calculated from the flow rate using $U_o = Q/A$. The sampling run-times for 1 L/min (1.46 cm/sec), 3.5 L/min (5.12 cm/sec), and 7 L/min (10.23 cm/sec) were 5 minutes, 1 minute, and 1 minute, respectively.

3.4 Magnetic Field

Permanent magnets were used to produce an approximately uniform magnetic field perpendicular to the direction of flow. Six 2"x2"x1" magnet blocks were placed around the filter holder with three stacked on one side and the remaining three on the opposite side as shown in Figure 3.2. 12 cm and 15 cm spacings produced magnetic field strengths of 100 mT and 50 mT, respectively, at the midpoint between the magnets. Figure 3.3 illustrates the magnetic field distribution with respect to the spacing between the magnets. As mentioned

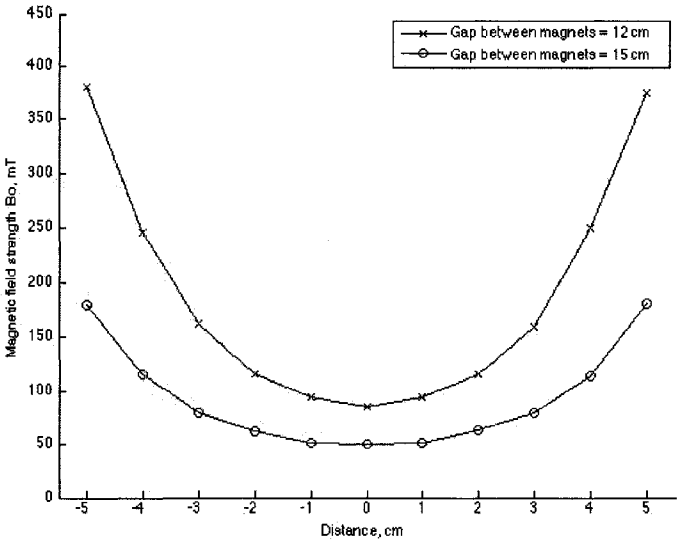

Figure 3.3: The magnetic field strength between permanent magnets spaced 12 cm and 15 cm apart. $x = 0$ is centered at the midpoint between the magnets and the center of the filter

in Section 2.3.3, a uniform magnetic field was assumed. However, as seen in the Figure 3.3, the 1.5" region centered in the middle of the filter, the magnetic field does vary. The measured magnetic field was fitted with a 4th order polynomial curve and a maximum gradient of 30 mT/cm was found near the circumference of the filter area. The significance of this magnetic field gradient and the force experienced by the particle are discussed in Chapter 4.

3.5 Challenge Mass and Efficiency

3.5.1 UV Mass Assay

The sampling filter and the Respirgard™ filters from a sampling run were washed with 0.1N NaOH solvent, which dissolved the cromoglycic acid from the surfaces of both filters. The absorbance, A_λ, of dissolved cromoglycic acid in NaOH, measured with an HP 8452A Diode Array Ultra-Violet Spectrophotometer, was correlated to the concentration of cromoglycic acid, C_{CG} in solution using Equation 3.1.

$$C_{CG} = \left(\frac{1}{0.9142}\right)(145.58 \times A_\lambda + 0.1939) \tag{3.1}$$

Equation 3.1 was determined using a linear regression analysis on the absorbance of standard samples of known concentrations of cromoglycic acid dissolved in 0.01N NaOH. The procedure for the washing of the nylon net filter remained constant across all sampling runs, but different extraction volumes were used for washing the Respirgard™ filter for the three face velocities. Table 3.2 summarizes the extractions used to dissolve cromoglycic acid off of the nylon net filter and Respirgard™ at various flow rates.

The procedure for preparation of extractions from the nylon net filter for examination is as follows. The nylon net filter was removed from the filter housing and placed into a crystallization dish. 5 mL of 0.01N NaOH was measured and poured into the crystallization dish. A pipette was used for

Table 3.2: Summary of the extractions and amount of 0.01N NaOH used for washing the nylon net filter and Respirgard™ for the different sampling flow rates

Sample	0.01N NaOH for the Sampling Face Velocity		
	1.46 [cm/sec]	**5.12 [cm/sec]**	**10.23 [cm/sec]**
Net Filter	2 × 5 mL	2 × 5 mL	2 × 5 mL
Respirgard	3 × 5 mL	1 × 10 mL 2 × 5 mL	1 × 10 mL 2 × 5 mL

spraying the 0.01N NaOH solvent over the surface of the nylon net filter 100 times. The remaining solution in the crystallization dish was then pipetted from the dish into a 5 mL volumetric flask and topped off to 5 mL. A second extraction was prepared using the same procedure as above.

The procedure for the preparation of extractions from the downstream Respirgard™ filter for examination by the UV spectrophotometer is as follows. The Respirgard™ filter and housing are shown in Figure 3.4. 5 mL 0.01N NaOH was measured and poured into the upstream opening of the Respirgard™ filter. The Respirgard™ filter was then placed onto the vibrating surface of a pressure activated shaker. By introducing vibration, the solvent could penetrate the pores of the Respirgard™ filter and reach the fibers captured there. The solution was pipetted out of the Respirgard™ filter into either 5 mL or 10 mL volumetric flasks (Table 3.2), depending on the sampling face velocity for that run and filled to the desired volume with NaOH. The preparation of the second and third 5 mL extractions were completed using the same procedure above.

The two extractions from the nylon net filter and the three extractions from the Respirgard™ filter were analyzed using the UV spectrophotometer. To begin the analysis, a blank sample of 0.01N NaOH was placed into a cuvette

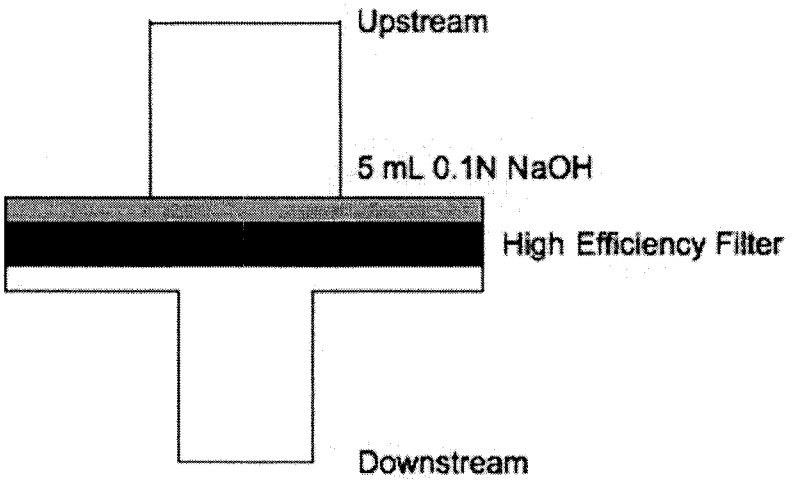

Figure 3.4: The Respirgard is depicted above with 5 mL 0.01N NaOH upstream of the high efficiency filter

to calibrate the baseline signal from the spectrophotometer. Each sample tested for the absorbance of the maximum wavelength, 324 μm to 328 μm and baseline wavelength, 296 μm to 298 μm. C_{CG}, the concentration of cromoglycic acid for each extraction was calculated from the difference between the upper and baseline absorbance, A_λ, and Equation 3.1, and the mass of cromoglycic acid from Equation 3.2. The total mass collected on the sampling filter and Respirgard™ filter, M_f and M_R respectively, was calculated as the sum of mass from all corresponding extractions.

$$m_{CG} = C_{CG} \times Vol_{extraction} \tag{3.2}$$

The overall efficiency, $\mathbf{E_{sample}}$ of the sampling filter challenged with cromoglycic acid fibers was given by Equation 3.3 and overall penetration, $\mathbf{P_{sample}}$ was given by Equation 3.4.

$$\mathbf{E_{sample}} = \frac{M_f}{M_{challenge}} = \frac{M_f}{M_f + M_R} \tag{3.3}$$

$$\mathbf{P_{sample}} = 1 - \mathbf{E_{sample}} = \frac{M_R}{M_f + M_R} \tag{3.4}$$

M_f and M_R are given above from Equation 3.2.

3.6 Fiber Count Protocol and Fiber Concentration

The experimental samples were prepared from the upstream Millipore™ membranes (0.2 μm GTP and 47 mm in diameter) for viewing under scanning electron microscope (JEOL 6301F, Field Emission Scanning Electron Microscope, SEM). The membrane filter was placed in the filter housing in the upstream sampling apparatus shown in Figure 3.2. Similar to the procedure in Section 3.3.1, the nebulizer and vacuum pump were run for one minute with the 3-way valve directing flow into the blank line before diverting flow to the main testing line for the experiment. Upstream samplings were run twice, each with a runtime of 30 seconds.

A sample image of the aerosol fibers is shown in Figure 3.5. To obtain a representation of the total population of fibers on a membrane, a minimum of 20 randomly selected viewing areas need to be taken, and in those 20 images, at least 100 fibers need to be counted according to NIOSH 7400 standards. Images were taken until either the number of viewing areas or the fiber count reaches 100. Fibers with a major dimension greater than 0.5 μm and an aspect ratio, β, greater than or equal to 3 were counted. Cromoglycic particles with a major dimension smaller than 0.5 μm generally had aspect ratios close to 1, so for the purpose of the experiment these particles were not considered during counting. Also, fibers that came into contact with the borders of the viewing area were not counted as they could not be properly sized. Filter efficiency of a poly-disperse, as opposed to a mono-disperse, aerosol is not the same when comparing by particle count and by mass. The total volume of the fibers

Figure 3.5: A sample of aerosol fibers captured on a Millipore membrane filter taken at a magnification of 1000x. The image was captured with scanning electron microscopy

(from particle counts) was needed for a proper comparison, therefore lengths and diameters of all fibers that appeared in the viewing areas were measured to give size distributions from upstream samples. The images had viewing areas of 321 μm^2 and the total area of the Millipore membrane exposed to the fibers was 1104 mm^2

3.7 Fiber Size Distribution

From the measured length and diameter distributions of each sample, the count median length and diameter, and the geometric standard deviations were determined. The geometric standard deviations, $\sigma_{g,L}$ and $\sigma_{g,D}$, for a lognormal count distribution of length and diameter, respectively, can be calculated from

Equation (3.5) and Equation (3.6).

$$\sigma_{g,L} = \frac{CML}{L_{16}} = \frac{L_{84}}{CML} \tag{3.5}$$

$$\sigma_{g,L} = \frac{CMD}{D_{16}} = \frac{D_{84}}{CMD} \tag{3.6}$$

CML is defined as the count median length at which 50% of the fiber count have a length less than this value. L_{16} and L_{84} are defined as the lengths at which 16% and 84% of the fiber count have length less than this value. Similarly, CMD is defined as the count median diameter at which 50% of the fiber count have a diameter less than this value. D_{16} and D_{84} are defined as the diameters at which 16% and 84% of the fiber count have a diameter less than this value.

3.8 Fiber Penetration

The main objective of this experiment was to test for the overall penetration of all cromoglycic acid fiber sizes through the filter with and without a magnetic field. Also, of particular importance for a poly-disperse aerosol is the size specific filtering efficiency. The overall and size specific penetrations could not be calculated straight from a comparison of the number concentrations of the upstream and downstream fiber samples since the samples were obtained on separate runs. Instead, the upstream and downstream fiber volume distributions were first put into size bins and normalized by the respective total volumes using a cylindrical approximation (Equation 3.7 and Equation 3.8.

$$V_{US,norm,l1-l2} = \frac{\int_{l1}^{l2} n_{US}(l) v_{US}(l) dl}{V_{US}} \tag{3.7}$$

$$V_{DS,norm,l1-l2} = \frac{\int_{l1}^{l2} n_{DS}(l) v_{DS}(l) dl}{V_{DS}} \tag{3.8}$$

$V_{US,norm,l1-l2}$ and $V_{DS,norm,l1-l2}$ represent the upstream and downstream normalized volume distributions for the $l1$ to $l2$ size bin. n_{US} and v_{US} are the

number concentration function and volume function for the upstream fiber sample and n_{DS} and v_{DS} are the number concentration function and volume function for the downstream fiber sample. Overall penetration, $\mathbf{P_{exp}}$, found using Equation 3.4, was used to find V_{DS} in terms of V_{US}. Upon substitution into Equation 3.8, $V_{DS,norm,l1-l2}$ was also found in terms of V_{US}. The penetration of a specific fiber length bin is then given by Equation 3.9.

$$\mathbf{P_{l1-l2}} = \frac{V_{DS,norm,l1-l2} \times M_{DS}}{V_{US,norm,l1-l2} \times M_{US}} \tag{3.9}$$

As the fiber size distributions were polydisperse ($\sigma_g \gtrsim 1$), the size specific penetration of the cromoglycic acid fibers through nylon net filters was determined. To accomplish this, the lengths and diameters of the counted fibers were organized into size bins, and the penetration of each bin was calculated according to Equation (3.9).

Chapter 4

Results and Discussion

4.1 Upstream Fiber Distributions

SEM images from upstream aerosol samples were analyzed to determine the size distributions. The aerosol was prepared with 20% by mass of magnetite. Fibers were counted and sized according to the procedure described in Section 3.6. 493 and 417 fibers were counted from the first and second upstream sampling runs. The count median lengths and diameters, geometric standard deviations, and volumetric median lengths and diameters of the samples are shown in Table 4.1. The fiber count, CML, CMD, and values for

Table 4.1: The distribution of cromoglycic acid fibers, loaded with magnetite particles, upstream of filters

Run	CML	σ_{gL1}		CMD	σ_{gD1}		VML	VMD
	$[\mu m]$		$\pm$	$[\mu m]$		$\pm$	$[\mu m]$	$[\mu m]$
1	1.89	1.60	0.10	0.38	1.45	0.05	2.99	0.54
2	1.89	1.63	0.10	0.40	1.48	0.10	2.97	0.56

geometric standard deviation were similar between sampling runs. σ_{gL} and σ_{gD}, as mentioned in Section 3.7, could be calculated in two ways. ie. the ratio of CML to L_{16}, and L_{84} to CML. The geometric standard deviations

in Table 4.1 were calculated as the average of these two values. The standard deviations of σ_{gL} and σ_{gD}, respectively, were found to be 0.10 and 0.05 for the first run, and 0.10 and 0.10 for the second run. In view of the nature of the counting protocol and the difficulty in controlling the amount of aerosol leaving the nebulizer, the distribution for both samples was consistent.

The parallel and perpendicular aerodynamic diameters were calculated using CMD and CML as discussed previously and are shown below in Table 4.2. The aerodynamic diameters for parallel orientation were larger than for

Table 4.2: The parallel and perpendicular aerodynamic diameters of fibers calculated with CMD and CML from size distributions of the sampling aerosol obtained with $U_o = 1.46\ cm/sec$ and 20% magnetite composition

% Magnetite	Particle Orientation	
	Parallel $\parallel$	Perpendicular $\perp$
10%	0.994	0.879
20%	1.024	0.906
30%	1.048	0.927

perpendicular orientations at all magnetite compositions. Consequently, aligning a fiber perpendicular to flow displayed effects of increasing diffusion and interception while decreasing impaction. These values were used in the calculation of the theoretical filtration through the nylon net filter challenged with cromoglycic acid and magnetite composite particles.

4.2 Magnetic and Aerodynamic Torque

The aerodynamic torque, $T_{ae,x}$ (Equation 2.22), was calculated with $G = 10230/sec$ for the largest face velocity of 10.23 cm/sec tested. G, was estimated as a linear gradient in the velocity from the center to the edge of a pore. The

magnetic torque, T_m (Equation 2.26), was calculated with $\mu_o H_o = 100\ mT$, and the saturation magnetization of magnetite, $M = 4.7 \times 10^5\ A/m$. l_f and d_f, in the expressions for $T_{ae,x}$ and T_m, were substituted with CML and CMD from upstream fiber distribution samples.

The ratio of magnetic and aerodynamic torque is plotted against the relative spacing of the magnetite particles in Figure 4.1. The magnetic torque was

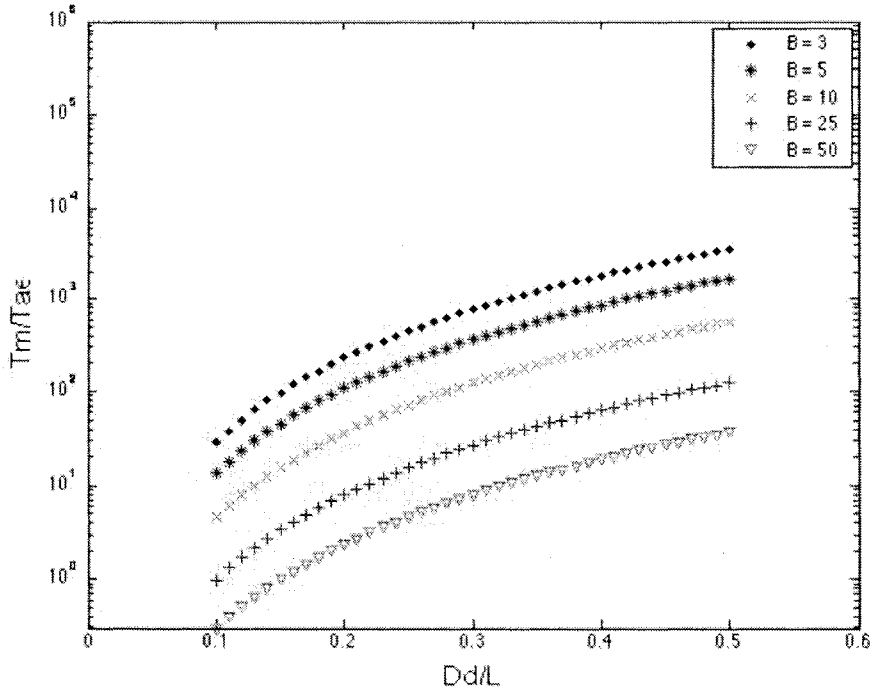

Figure 4.1: The ratio of the magnetic and aerodynamic torque on the fiber particle was plotted against the magnetic material spacing for various aspect ratios, β. A velocity gradient, G, was estimated at $10230/sec$. The magnetic field strength was $\mu_o H_o = 100\ mT$.

larger than the aerodynamic torque for magnetite spacings, d_d/L, from 0.1 to 0.5. The ratio, T_m/T_{ae}, increased with higher aspect ratio and magnetite spacing. The aspect ratio of a particle with the CML and CMD from the upstream

aerosol sample was approximately equal to 5. At this aspect ratio, T_m/T_{ae} was found to be approximately 10 at $d_d/L = 0.1$ and 1000 at $d_d/L = 0.5$ indicating that magnetic torque was sufficient to align the particles.

4.3 Experimental Mass Efficiencies

For a face velocity of $U_o = 1.46\ cm/sec$, the experimental mass efficiencies, for 0, 50, and 100 mT magnetic fields, and 10%, 20%, and 30% magnetite compositions (by mass), are shown in Table 4.3. There was little indication that challenge mass affected filtering efficiency, which raised confidence that the differences in the challenge mass were not a contributing factor to the observed changes in filtering efficiencies.

Table 4.3: Filter Efficiencies [%] obtained from the testing of the filter using a face velocity of $U_o = 1.46\ cm/sec$, various field strengths and magnetite compositions.

% Magnetite	Magnetic Field Strength $[mT]$		
Composition	0	50	100
10	10.94 ± 2.27	18.18 ± 3.08	17.31 ± 1.62
20	13.30 ± 2.35	19.88 ± 0.48	27.87 ± 0.23
30	17.08 ± 0.99	23.95 ± 1.97	37.13 ± 3.00

In the case of 10% mass composition of magnetite, the filter efficiency without a magnetic field in place was found to be 10.94±2.27%. Efficiencies of 18.18±3.08% and 17.31±1.62% were observed when the magnetic field strength was increased to 50 mT and 100 mT, respectively. A one-tailed t-test was performed on each of the data sets to determine statistical differences between the samples, with and without the magnetic field. Both cases were found to be statistically significant when a $p < 0.05$ criteria was used ($p = 0.014$ and $p = 0.014$). The data indicates that fiber alignment had become saturated

since efficiency remained nearly constant between the sampling runs for the latter two magnetic field strengths.

For the next set of sampling runs, also shown in Table 4.3, the mass composition of magnetite was increased to 20%. Without an applied magnetic field the efficiency was $13.30 \pm 2.35\%$. At 50 mT, the filter efficiency was $19.88 \pm 0.43\%$, and at 100 mT, the filter efficiency increased further to $27.87 \pm 0.23\%$. Using the same statistical t-test from above, the differences in efficiency for 50 mT and 100 mT runs, were found to be statistically significant with $p = 0.03$ and $p = 0.006$.

For a magnetite composition of 30%, the effect of the magnetic field on the filtration was further enhanced. At 0 mT, efficiency was $17.08 \pm 0.99\%$. The efficiency increased to $23.95 \pm 1.97\%$ for a magnetic field strength of 50 mT and further increased to $37.13 \pm 3.00\%$ for a magnetic field strength of 100 mT. These changes were found to be statistically significant with $p = 0.024$ and $p = 0.006$ for 50 and 100 mT, respectively. Contrasting to 10%, the efficiencies for the 20% and 30% sampling runs did not approach a constant value for increased field strength. Further discussion of this data will follow in Section 4.4.

Table 4.4: Filter Efficiencies [%] obtained from the testing of the filter using a face velocity of $U_o = 5.12$ cm/sec, and various field strengths and magnetite compositions.

% Magnetite	Magnetic Field Strength $[mT]$		
Composition	0	50	100
10	12.64 ± 1.58	-	13.15 ± 0.97
20	11.18 ± 0.45	15.25 ± 0.77	14.84 ± 0.37
30	13.30 ± 1.22	19.08 ± 1.13	17.35 ± 0.45

The mass filter efficiencies were obtained for a face velocity of $U_o = 5.12$ cm/sec and are summarized in Table 4.4. For a magnetite composition of

10% and without a magnetic field, the filter efficiency was 12.64 ± 1.58%. Compared to 10.94 ± 2.27% obtained for $U_o = 1.46\ cm/sec$, there was no statistical difference between the data samples. Upon application of the 100 mT, efficiency did not change ($p = 0.413$). For magnetite compositions of 20% and 30%, the filtering efficiency increased when the 50 mT field was applied but did not increase further for the 100 mT.

Finally, the filtration efficiencies for a face velocity of 10.23 cm/sec are shown in Table 4.5. For all magnetite compositions, filtration efficiency did not change when the 100 mT magnetic field was applied.

Table 4.5: Filter Efficiencies [%] obtained from the testing of the filter using a face velocity of $U_o = 10.23\ cm/sec$, and various field strengths and magnetite compositions.

% Magnetite	Magnetic Field Strength [mT]		
Composition	0	50	100
10	13.99 ± 1.68	-	14.89 ± 0.62
20	14.98 ± 1.41	-	11.76 ± 1.59
30	17.57 ± 0.06	-	17.79 ± 2.06

In order to make an interpretation on the alignment of the fibers and their consequent effect on filtration, the trends of the experiment are summarized here. At $U_o = 1.46\ cm/sec$, there was a significant increase in the filtration efficiency of the fibers when the magnetic field was placed perpendicular to the flow. This trend was observed for all magnetite compositions. A further increase was detected as the magnetic field strength increased at the higher 20% and 30% compositions, however, efficiency stayed the same at the lower 10% composition. For 5.12 cm/sec, increases from the baseline filtration were only observed for 20% and 30% compositions. At 10% composition however, efficiency did not change upon applying the field. Finally, at the face velocity, 10.23cm/sec, the data showed no differences in filtration efficiencies when the

magnetic field was applied. At first glance, the data seemed to indicate that for 10.23 cm/sec, fibers were only exhibiting partially or no alignment at all. However, fibers appeared to align on membrane filters at the three face velocities, shown below in Figure (4.2). The forthcoming sections, single-fiber theory will be examined to provide understanding of the resulting trends.

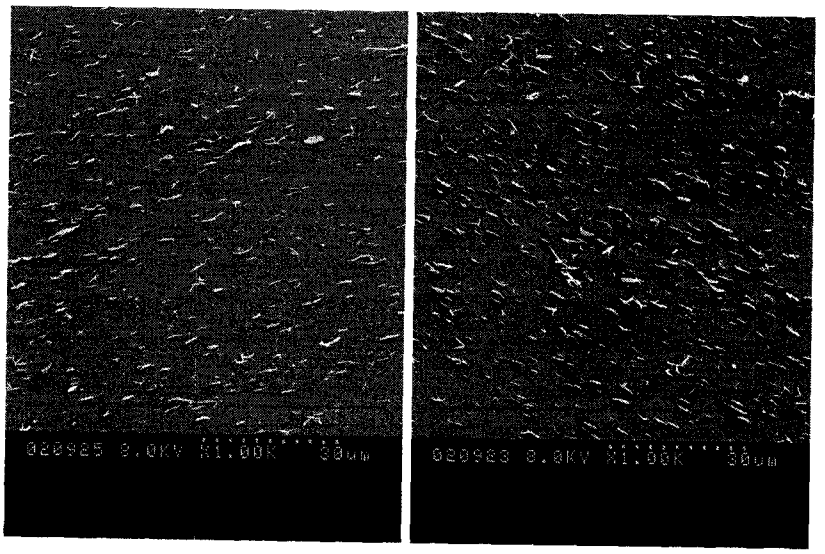

(a) $U_o = 1.46\ cm/sec$ (b) $U_o = 5.12 cm/sec$

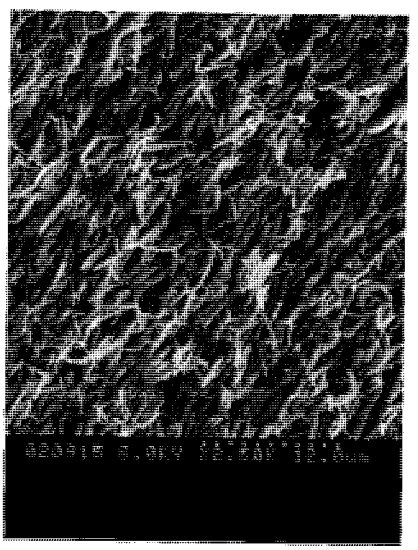

(c) $U_o = 10.23 cm/sec$

Figure 4.2: Alignment of fibers, prepared with 10% magnetite composition, captured with $0.2\mu m$ pore size membrane filters as shown in SEM images. The 100 mT magnetic field was used.

4.4 Single-Fiber Efficiency Comparison

The single-fiber efficiency and theoretical filtration were calculated using $CML = 1.89\mu m$ and $CMD = 0.39\mu m$ from the aerosol samples obtained under the following conditions: $U_o = 1.46\ cm/sec$ and a 20% magnetite composition (Section 4.1). In each of the Figures 4.3 - 4.11, the experimental mass efficiencies were plotted against the magnetic field strength. The theoretical efficiencies were plotted on the same figures for reference, but there is no relationship between those values and magnetic field strength. Also in part b) of each figure, the single-fiber efficiency was divided so that the contributions of the basic deposition mechanisms could be distinguished. The density of the particles used were $\rho = 1629\ kg/m^3$, $\rho = 1713\ kg/m^3$, and $\rho = 1813\ kg/m^3$ corresponding to 10%, 20%, and 30% magnetite composition cases, respectively.

Single-fiber theory predicted the general trend of efficiency changes without a magnetic field in place as face velocity was adjusted. Referring to Figures 4.3(a) and 4.6(a), the baseline filtration efficiencies did not differ statistically (standard one-tailed t-test with $p = 0.200$). In comparison, only a slight decrease in overall efficiency from 14.5% to 13.3% for parallel alignment was predicted by single-fiber theory. Interception and diffusion were the major contributors to the overall efficiency (Figure 4.3(b)) for the lower face velocity, while interception and impaction were major contributors for the higher face velocity (Figure 4.6(b)). At different flow regimes, the weightings of the deposition mechanisms can differ and still yield the same overall efficiency, which explains the trend seen here. At a face velocity of $10.23cm/sec$ (Figure 4.9(a)), the experimental efficiency was $13.99 \pm 1.68\%$ and theoretical efficiency for parallel orientation was 17.6%. Although the theoretical value was outside the range of the error bars, the trend of an increase in efficiency was seen.

From Figure 4.9(b), impaction for parallel particle alignment was the largest contributor to deposition, while diffusion's role decreased dramatically.

For $U_o = 1.46\ cm/sec$, single-fiber theory predicted filtration efficiencies higher for 10% and 20% magnetite compositions and lower for 30% (Figures 4.3, 4.4, and 4.5). At 10%, filtration efficiency appeared to approach a saturation value as the magnetic field strength increased, but this was not seen for 20% and 30% compositions. One possible explanation may be that there was only partial alignment of the fibers with the 50 mT field and further alignment with the 100 mT field. However, at higher velocity gradients (5.12 cm/sec) there was full alignment at 50 mT indicated by a saturation efficiency (Figures 4.7(a) and 4.8(a)), making it likely that a similar trend would be seen for the lower face velocity. The author is of the opinion that there was full alignment of the fibers, although the significance of gradients in the 100 mT magnetic field were underestimated. The gradient at the center of the filter was 0 mT/cm but was as high as 30 mT/cm near the circumference of the filter area. A crude estimate of the distance travelled by the particle through the filter was approximated using equation 2.29, as well as simple kinetic and kinematic equations. The mass and densities of cromoglycic acid and magnetite were known so that the volume fraction of magnetite, χ_{frac}, could be calculated. The distance travelled by the particle was found to be in the order of hundreds of micro-meters, and considering that the pore size was only $20\mu m$, this distance was significant. The efficiencies found for 100 mT and 20%/30% are ignored for the remainder of the discussion.

The efficiencies for the conditions at 1.46 cm/sec and 10% magnetite composition (Figure 4.3) were over-valued by theoretical calculations. The single-fiber efficiencies for parallel and perpendicular orientations were found to be 14.51% and 22.01%. The sampling runs for the combination of $U_o = 1.46$ cm/sec and 20% magnetite compositions are shown in Figure 4.4. Experimen-

tal efficiency changed from $13.30 \pm 2.35\%$ (no magnetic field) to $19.88 \pm 0.43\%$ (50 mT magnetic field) while theory predicted 14.47% for the unaligned case, and 21.82% for the aligned case. The impact of fiber orientation on the capture efficiency was seen through the breakdown of single-fiber efficiency (Figure 4.3, 4.4, and 4.5). The changes in interception from unaligned to aligned cases, remained constant for all face velocities since its dependence was only on the geometry of the particle and pores. The changes in impaction, sedimentation, and to a lesser extent sedimentation were not only influenced by the fiber orientation, but by face velocity and particle density as well. Taking note of the significance of diffusion versus impaction, the decrease in E_{imp}, between the unaligned and aligned cases paled in comparison to the increases in E_{int} and E_{diff}. The theoretical calculations suggest that the overall efficiency increase from the unaligned to aligned orientations was a result of the increases in diffusion and interception.

For the face velocity of $5.12 cm/sec$ (Figures 4.6, 4.7, and 4.8) there were noticeable increases in the efficiencies for 20%, 30%, but not 10% magnetite compositions. The filtration efficiency of 20% and 30% compositions approached saturated values of $15.05 \pm 1.14\%$ and $18.22 \pm 1.58\%$ as magnetic field strength increased. The theoretical predictions were outside of error bars for unaligned and aligned orientations in the 20% case, and in fairly good agreement for both orientations in the 30% case. For parallel alignment the major contributions to deposition were through interception, diffusion, and inertial impaction, with the latter having the largest weighting. In comparison, theoretical calculations for perpendicular orientation showed that the largest contribution was from interception. The changes in impaction were substantial in contrast to those observed for 1.46 cm/sec, but because interception changes were even larger, there was still an overall efficiency increase as a result of fiber alignment. As expected, the role of impaction became larger and the role of diffusion became

smaller as a result of increased face velocity.

As face velocity was further increased to 10.23 cm/sec (Figures 4.9, 4.10, and 4.11), the magnetic alignment no longer held a noticeable impact on the overall filtration efficiency. Impaction was the largest contributor compared to interception and diffusion, for parallel alignment. When the magnetic field was put into place, the increase in interception was balanced by the decrease in impaction, resulting in the same efficiency as in the unaligned case. Unlike experimental results, there was an increase in overall efficiency predicted by theory. However, this data indicated that if face velocity was further increased, the effect of alignment leading to increased interception would likely be dominated by a decrease in impaction. There would also be a face velocity and Stk number at which an expected decrease in filtration due to magnetic alignment would be seen.

The agreement in overall efficiencies between theoretical calculations and experimental results is mixed. There was fairly good agreement for sampling runs with the parameters 1.46 and 5.12 cm/sec at all magnetite compositions, but theoretical predictions consistently valued higher efficiencies compared to experimental results at the higher 10.23 cm/sec. Still, single-fiber expressions was useful to provide rough estimates of the overall efficiencies and insight into the deposition mechanisms involved.

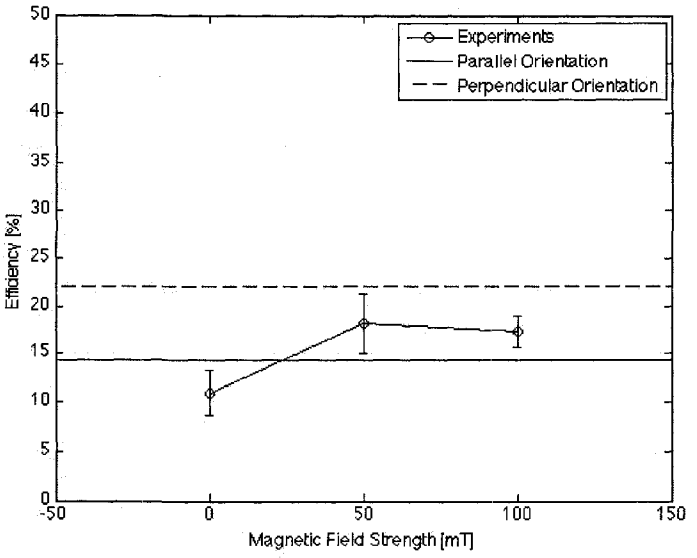

(a) 10% magnetite

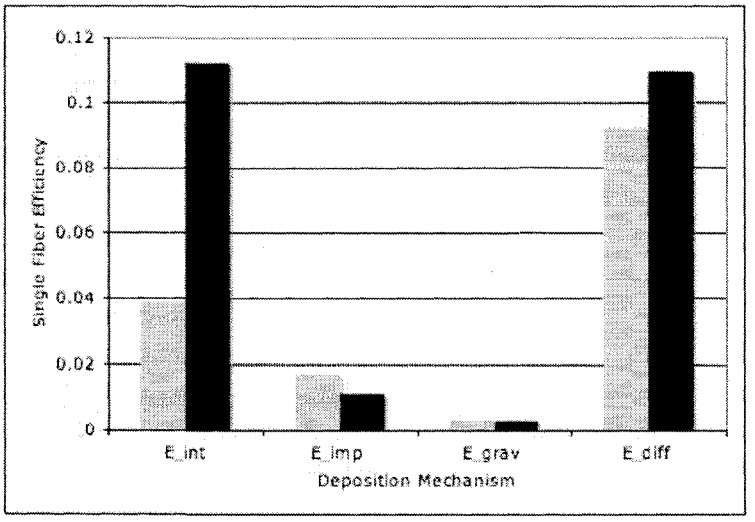

(b) Single-fiber theory for deposition mechanisms. Grey - parallel alignment. Black - perpendicular alignment

Figure 4.3: Mass efficiency of the nylon net filter with and without the influence of the magnetic field. $U_o = 1.46\ cm/sec$ and 10% magnetite

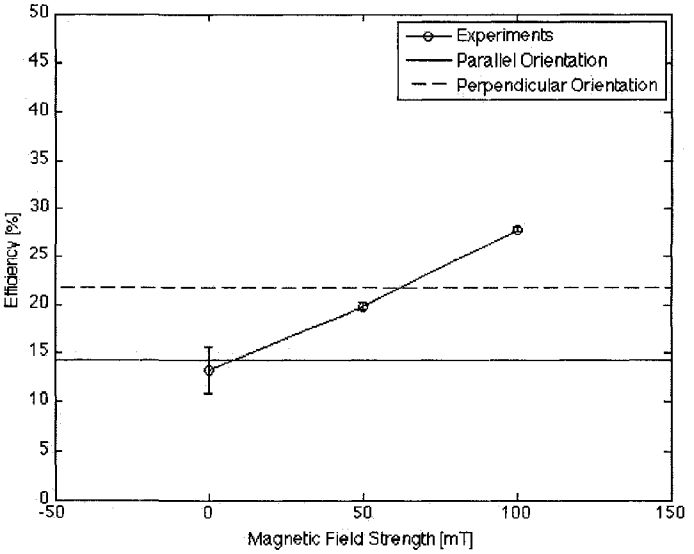

(a) 20% magnetite

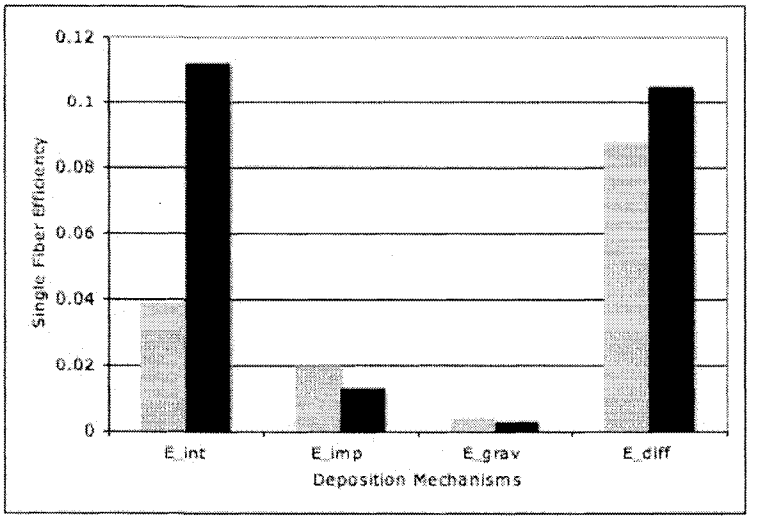

(b) Single-fiber theory for deposition mechanisms. Grey - parallel alignment. Black - perpendicular alignment

Figure 4.4: Mass efficiency of the nylon net filter with and without the influence of the magnetic field and a comparison to single-fiber theory. $U_o = 1.46\ cm/sec$ and 20% magnetite

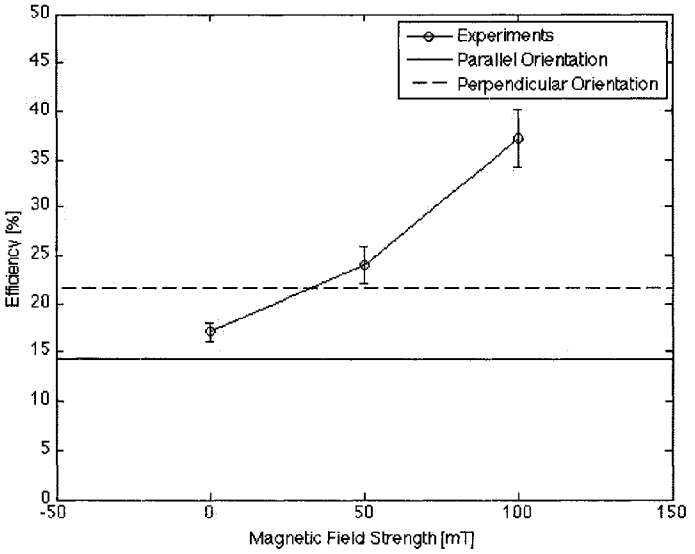

(a) 30% magnetite

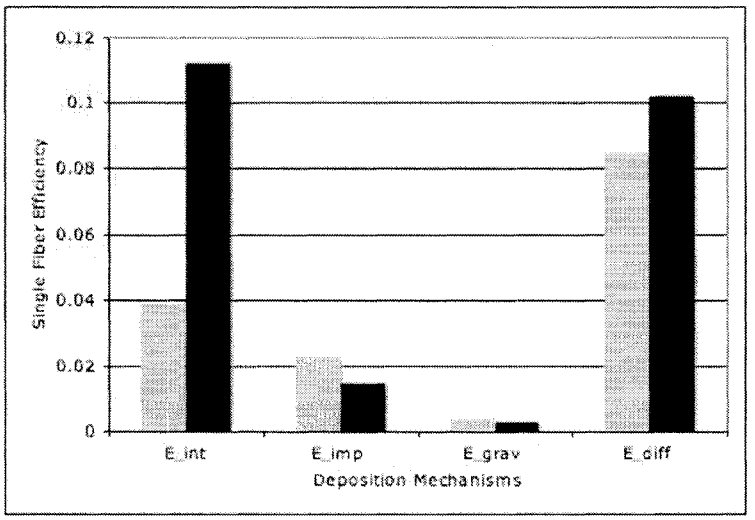

(b) Single-fiber theory for deposition mechanisms. Grey - parallel alignment. Black - perpendicular alignment

Figure 4.5: Mass efficiency of the nylon net filter with and without the influence of the magnetic field and a comparison to single-fiber theory. $U_o = 1.46\ cm/sec$ and 30% magnetite

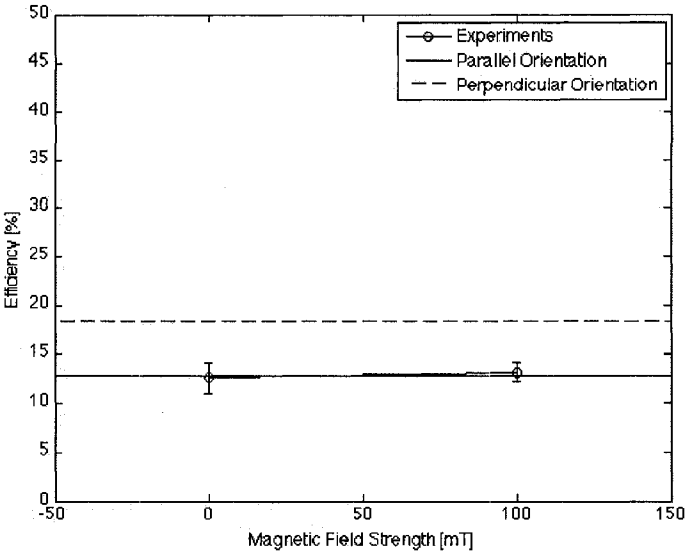

(a) 10% magnetite

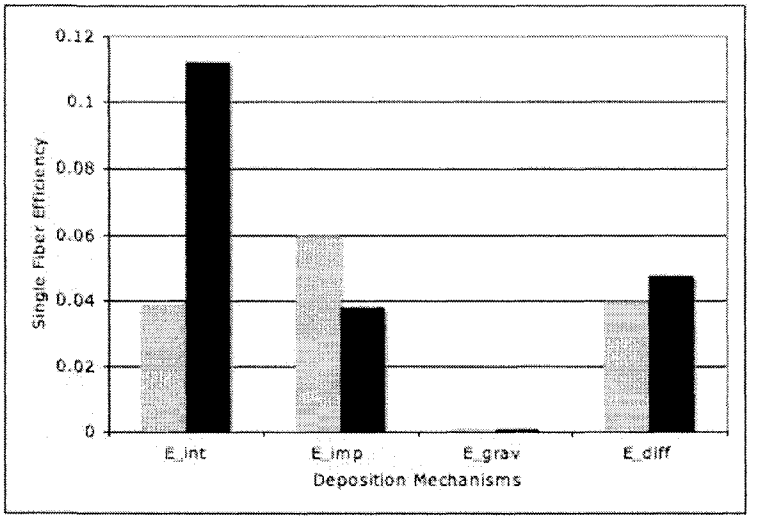

(b) Single-fiber theory for deposition mechanisms. Grey - parallel alignment. Black - perpendicular alignment

Figure 4.6: Mass efficiency of the nylon net filter with and without the influence of the magnetic field and a comparison to single-fiber theory. $U_o = 5.12 cm/sec$ and 10% magnetite

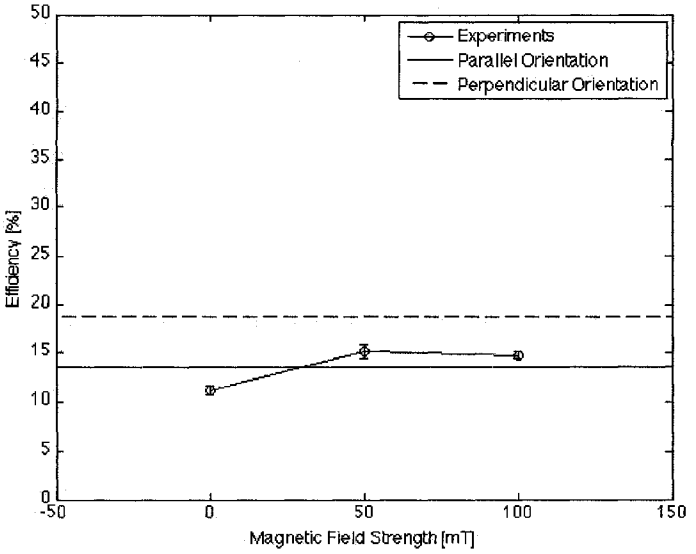

(a) 20% magnetite

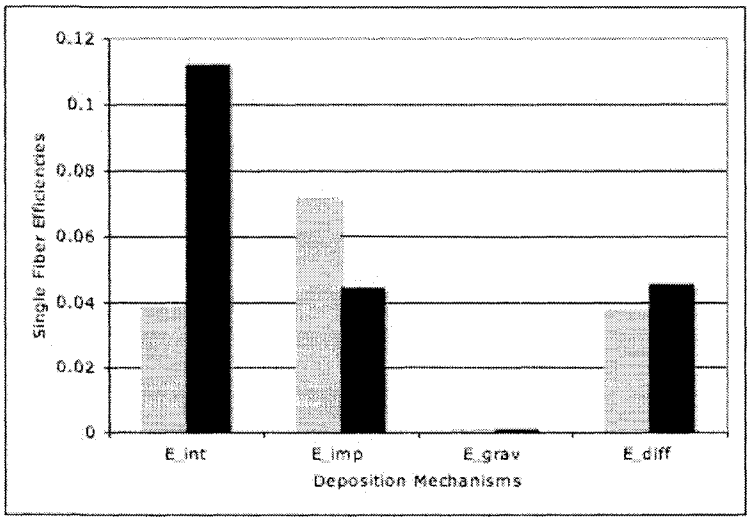

(b) Single-fiber theory for deposition mechanisms. Grey - parallel alignment. Black - perpendicular alignment

Figure 4.7: Mass efficiency of the nylon net filter with and without the influence of the magnetic field and a comparison to single-fiber theory. $U_o = 5.12 cm/sec$ and 20% magnetite

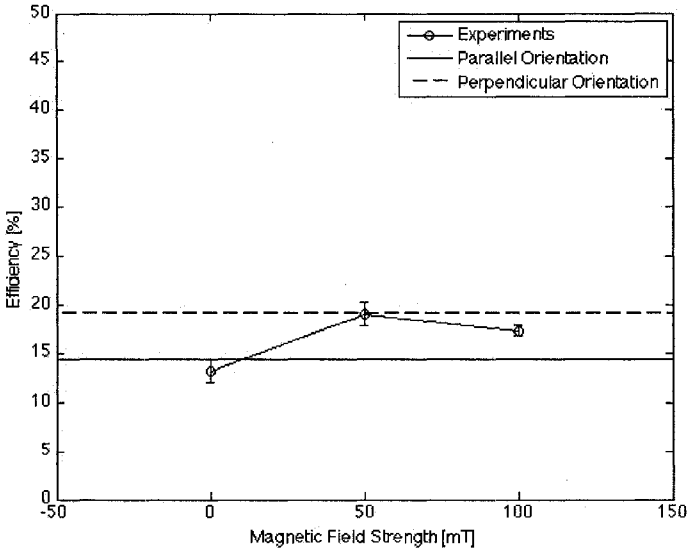

(a) 30% magnetite

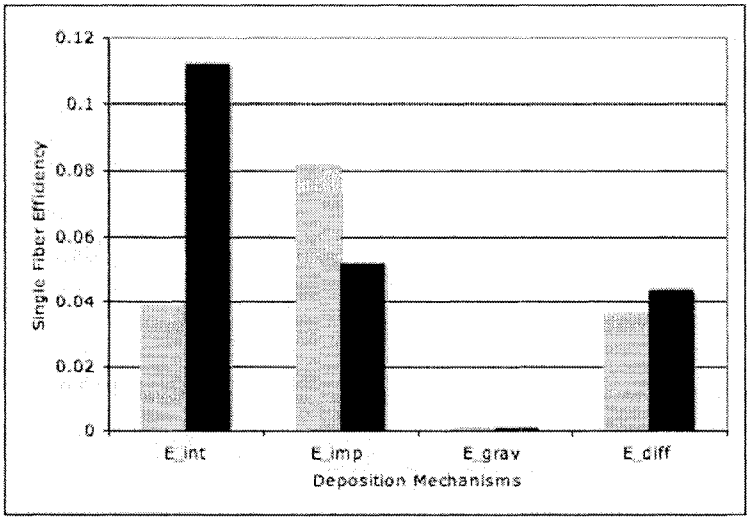

(b) Single-fiber theory for deposition mechanisms. Grey - parallel alignment. Black - perpendicular alignment

Figure 4.8: Mass efficiency of the nylon net filter with and without the influence of the magnetic field and a comparison to single-fiber theory. $U_o = 5.12cm/sec$ and 30% magnetite

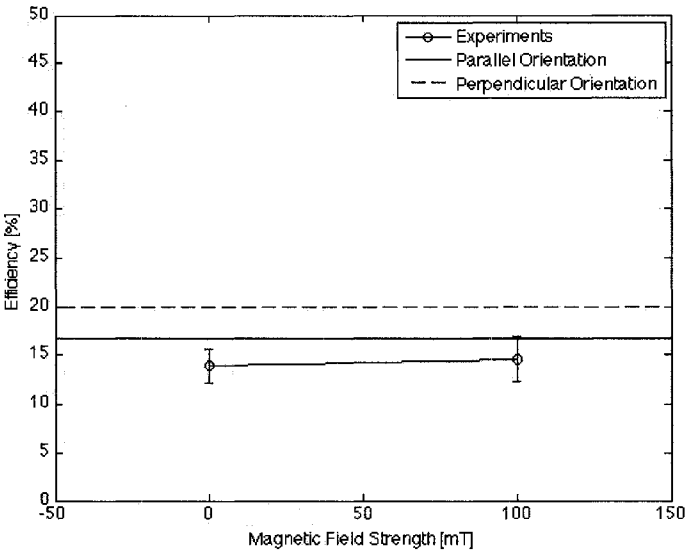

(a) 10% magnetite

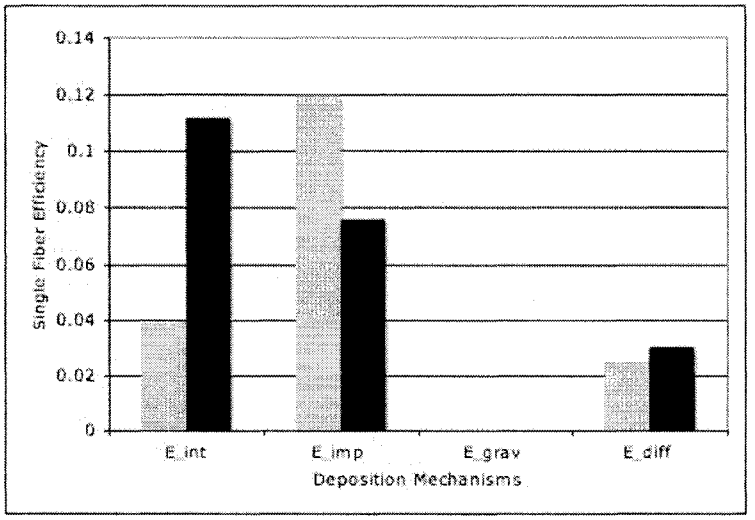

(b) Single-fiber theory for deposition mechanisms. Grey - parallel alignment. Black - perpendicular alignment

Figure 4.9: Mass efficiency of the nylon net filter with and without the influence of the magnetic field and a comparison to single-fiber theory. $U_o = 10.23 cm/sec$ and 10% magnetite

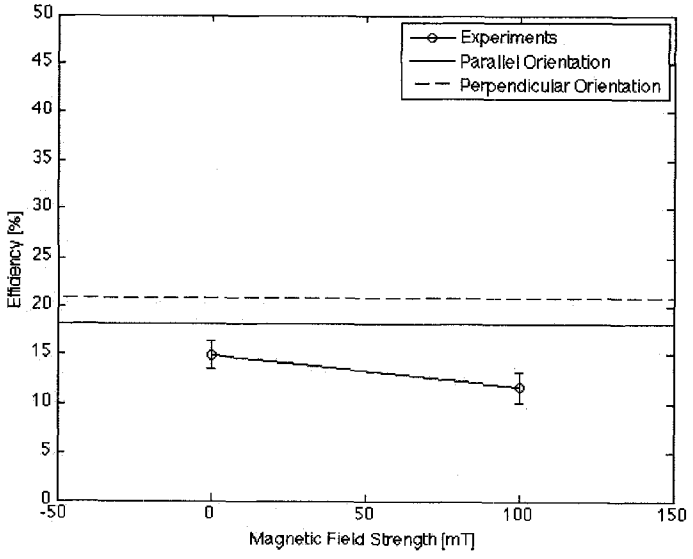

(a) 20% magnetite

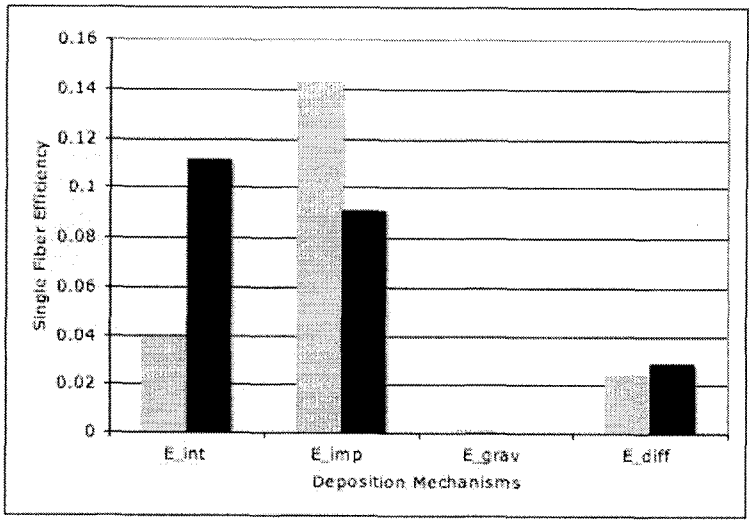

(b) Single-fiber theory for deposition mechanisms. Grey - parallel alignment. Black - perpendicular alignment

Figure 4.10: Mass efficiency of the nylon net filter with and without the influence of the magnetic field and a comparison to single-fiber theory. $U_o = 10.23 cm/sec$ and 20% magnetite

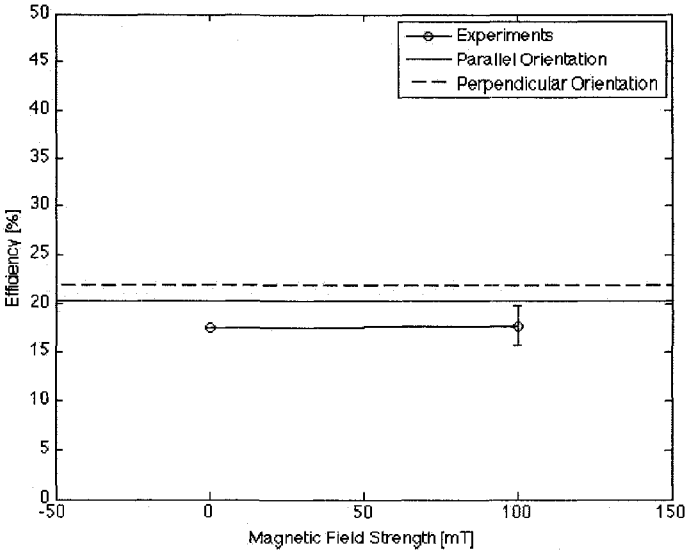

(a) 30% magnetite

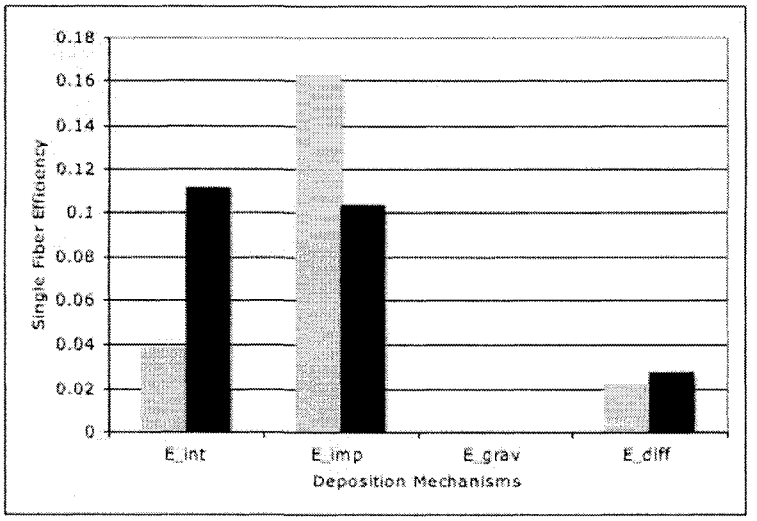

(b) Single-fiber theory for deposition mechanisms. Grey - parallel alignment. Black - perpendicular alignment

Figure 4.11: Mass efficiency of the nylon net filter with and without the influence of the magnetic field and a comparison to single-fiber theory. $U_o = 10.23 cm/sec$ and 30% magnetite

4.5 Size Specific Fiber Penetration

The size distribution from Section 4.1 was categorized into length bins with the count median length and diameter obtained for each. These count median values were used to determine the mass efficiency, and upstream and downstream distributions for each size bin as shown in Figures 4.12(a) and 4.12(b). The mass efficiency curves for fibers filtered in unaligned or aligned orientations were found to dip between $l = 1\ \mu m$ and $l = 2\ \mu m$ and increase thereafter for larger lengths. Deposition by diffusion and interception were likely the dominant mechanical processes for the smaller fiber lengths, whereas impaction and interception were for larger fiber lengths. In all length categories the overall efficiency for perpendicular orientation was larger than for parallel orientation. The efficiency of aligned fibers diverged from that of unaligned fibers for larger length bins. For larger lengths in the aligned downstream distribution, however, the differences were small compared to the unaligned distribution since only a small fraction of the fibers were in that size category. The bulk of the aerosols mass had fiber lengths in the $1\mu m$ to $6\mu m$ range and experienced the largest filtration.

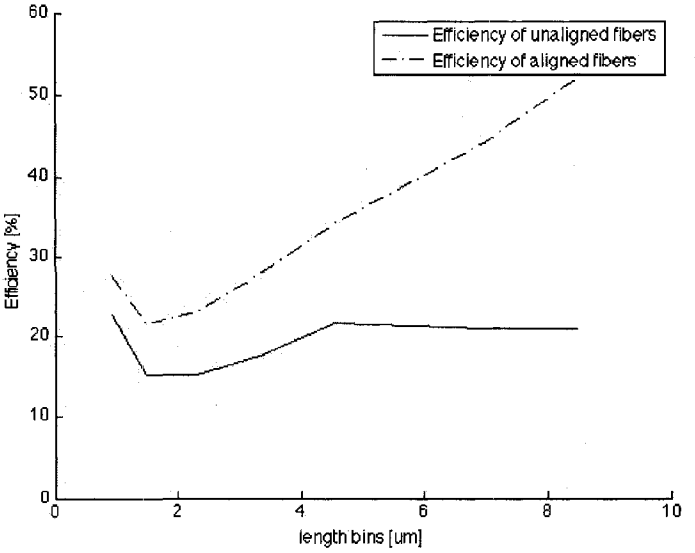

(a) Size specific mass efficiency

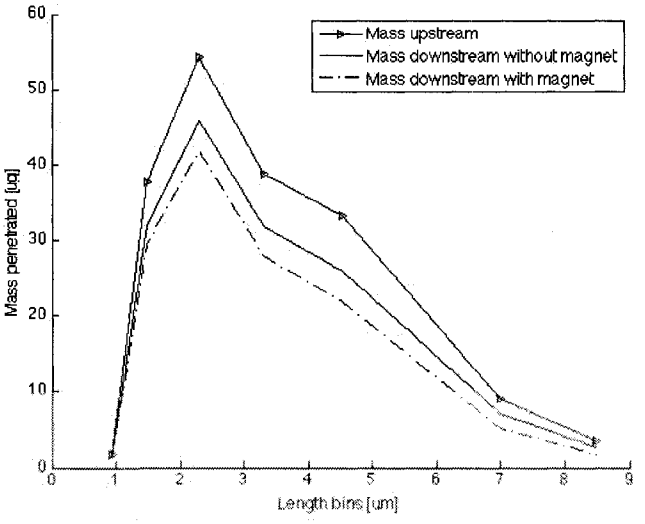

(b) Aerosol distribution downstream of nylon net filter

Figure 4.12: The size specific mass efficiency through the nylon net filter challenged with fibers, and the downstream distribution of fibers.

Chapter 5

Conclusion and Future Work

The magnetic alignment of fibrous aerosol particles increased the capture efficiency in a nylon net filter for certain operating regions. There was strong evidence of fiber alignment throughout the course of this research: The comparison of magnetic and aerodynamic torques showed that magnetic torque was orders of magnitude larger, saturation of efficiency occurred as magnetic field strength was increased, alignment of captured fibers was seen by SEM imaging, and efficiency increased when a magnetic field was applied. The magnetic properties of the fiber particles were attributed to the magnetite deposits on the surface of the cromoglycic acid material. Utilizing fiber counting procedures, the sampling aerosol had a lognormal size distribution with $CML = 1.89\ \mu m$, $CMD = 0.39\ \mu m$, $\sigma_{gL} = 1.62 \pm 0.10$, and $\sigma_{gD} = 1.47 \pm 0.07$. With this data, the parallel and perpendicular aerodynamic diameters were calculated and used along with single-fiber theory expressions to obtain capture efficiency in a filter.

Filtration efficiency of the nylon net filter was examined using standard techniques and ultra-violet mass measurement. Changing the face velocity, magnetite composition, and magnetic field strength had varying effects on filtration. At 1.46 cm/sec and all magnetite compositions, the data showed significant increases in filtration efficiency when 50 mT or 100 mT magnetic fields

were applied across the filter. Single-fiber theory attributed this enhanced capture to interception and diffusion. At 5.12 cm/sec, increased capture was only seen for 20% and 30% magnetite composition sampling runs under the influence of the magnetic field. Different operating conditions can have different weightings of inertial impaction, gravitational, diffusion, and interception resulting in the same overall filtrations. This was observed for 10.23 cm/sec sampling runs, in which filter increases were not seen under the influence of the magnetic field. Impaction here was the major deposition mechanism compared to interception and diffusion for the unaligned orientation, while interception dominated impaction and diffusion for the aligned fiber orientation. Single-fiber theory was in fairly good agreement with the results from 1.46 and 5.12 cm/sec sampling runs, but was inconsistent for 10.23 cm/sec. Fiber distributions may have differed from case to case, however, CML and CMD used were from one parameter combination and may explain the discrepancy between theoretical and experimental efficiencies. Another source of error may have been due to losses during the mass assay procedures which involved several extractions of the sampling filter and downstream filter. Lastly, particles could have been re-entrained back into the air after depositing, which could explain the higher efficiencies predicted by theoretical expressions.

A saturation efficiency was observed for increasing magnetic field strength for all parameter combinations except 1.46 cm/sec and 20%/30%. It was hypothesized that in addition to fiber alignment, there was also deposition through a magnetic force caused by gradients in the 100 mT magnetic field, which were significant for these sampling runs.

By organizing the fiber distribution into length bins, size specific efficiencies and downstream distributions were obtained. For relatively large lengths ($length > 4\ \mu m$), the mass efficiency for the aligned fibers diverged from the efficiency for the unaligned fibers. Since the larger fibers made up only a frac-

tion of the total aerosol, this change in mass of the size bin did not differ significantly.

5.1 Future Work

The work in this research was used to provide evidence that certain types of airborne asbestos fibers could align in the presence of a magnetic field, given that they exhibit magnetic anisotropy and similar magnetization as the cromoglycic acid and magnetite composite particle. Ulanowski and Kaye (1999) suggested that the magnetic alignment of asbestos fibers coupled with optical detection technology could potentially be utilized as a method to verify the presence of or to distinguish asbestos fibers.

Due to the onerous nature of manual fiber counting procedures to obtain the size distribution of fibrous aerosol, it is desirable to have an automated program that performs this analysis to ensure counting consistency and ease of recording. Fibers imaged can often appear in clumps and in random orientations that require objective reasoning to properly size, and therefore proves difficult to program. These difficulties can be partially alleviated for an aligned fiber distribution and with proper control of the magnetic field gradients, can be used to estimate the fiber distribution without a magnetic field.

Lastly, because of the dependence on length for interception, magnetic alignment can be used in conjunction with nylon net filters of various pore size as a pre-conditioner of a poly-disperse aerosol to obtain a mono-disperse one.

An understanding of the deposition mechanisms was gained through the examination of the theoretical and experimental work. For the aerosol used in the present study, magnetic alignment of fibers was seen as a viable solution to increasing filter efficiency.

References

I. Akira, K. Tanaka, H. Honda, S. Abe, H. Yamaguchi, and T. Kobayashi. Complete regression of mouse mammary carcinoma with a size greater than 15 mm by frequent repeated hyperthermia using magnetite nanoparticles. *Journal of Bioscience and Bioengineering*, 96(4):364–369, 2003.

J. Ally, B. Martin, M.B. Khamesee, W. Roa, and A. Amerfazli. Magnetic targeting of aerosol particles for cancer therapy. *Journal of Magnetism and Magnetic Materials*, 293:442–449, 2005.

B. Asgharian, L. Zhang, and C.P. Fang. Theoretical calculations of the collection efficiency of spherical particles and fibers in an impactor. *Journal of Aerosol Science*, 28(2):277–287, 1997.

R. Asmatulu, M.A. Zalich, R.O. Claus, and J.S. Riffle. Synthesis, characterization and targeting of biodegradable magnetic nanocomposite particles by external magnetic fields. *Journal of Magnetism and Magnetic Materials*, 292:108–119, 2004, 2005.

I. Balashazy, T.B. Martonen, and W. Hofmann. Fiber deposition in airway bifurcations. *Journal of Aerosol Medicine*, 3(4):243–260, 1990.

P.A. Baron and K. Willeke. *Aerosol Measurement: Principles, Techniques, and Applications.* Wiley-Interscience, Inc,, second edition, 2001.

D.M. Bernstein, J.M.R. Sintes, B.K. Ersboell, and J. Kunert. Biopersistence of synthetic mineral fibers as a predictor of chronic intraperitoneal injection tumor response in rats. *Inhalation Toxicology*, 13:851–875, 2001.

H.K. Chan and I. Gonda. Aerodynamic properties of elongated particles of cromoglycic acid. *Journal of Aerosol Science*, 20(2):157–168, 1989.

B.T. Chen, H.C. Yeh, and C.H. Hobbs. Size classification of carbon fiber aerosols. *Aerosol Science and Technology*, 19:109–120, 1993.

Y.K. Chen and C.P. Yu. Sedimentation of fibers from laminar flows in a horizontal circular duct. *Aerosol Science and Technology*, 14:343–347, 1991.

F.Y. Cheng, C.H. Su, Y.S. Yang, C.S. Yeh, C.Y. Tsai, C.L. Wu, C.L. Wu, M.T. Wu, and D.B. Shieh. Characterization of aqueous dispersions of Fe_3O_4 nanoparticles and their biomedical applications. *Biomaterials*, 26:729–738, 2005.

Y.S. Cheng, T.D. Holmes, and B. Fan. Evaluation of respirator filters for asbestos fibers. *Journal of Occupational and Environmental Hygiene*, 3: 26–35, 2006.

W.H. Finlay. *The Mechanics of Inhaled Pharmaceutical Aerosols.* Academic Press, 2001.

I. Gallily and A.H. Cohen. On the orderly nature of the motion of nonspherical aerosol particles: Inertial collision between a spherical large droplet and an axially symmetrical elongated particle. *Journal of Colloid and Interface Science*, 68(2):388–356, 1979.

J.W. Gentry, K.R. Spurny, J. Schormann, and R.J. Han. Filtration and diffusion of asbestos fibers: Comparison of experiment and theory. *Journal of Aerosol Science*, 21(1):711–714, 1990.

I. Gonda and A.F. Abd El. Khalik. On the calculation of aerodynamic diameters of fibers. *Aerosol Science and Technology*, 4:233–238, 1985.

R.L. Harris and D.A. Fraser. A model for deposition of fibers in the human respiratory system. *American Industrial Hygiene Association Journal*, 37: 73–89, 1976.

W.C. Hinds. *Aerosol Technology: Properties, Behavior, and Measurement of Airborne particles.* John Wiley and Sons, Ltd., 1982.

G.B. Jeffery. The motion of ellipsoidal particles immersed in a viscous fluid. *Proceedings of the Royal Society of London A102*, 161, 1922.

R. Lange, H. Fissan, and A. Schmidtt-Ott. Predicting the collection efficiency of agglomerates in fibrous filters. *Particle and particle systems characterization*, 16:60–65, 1999.

K.W. Lee and B.Y.H. Liu. Theoretical study of aerosol filtration by fibrous filters. *Aerosol Science and Technology*, 1:147–161, 1982.

A.R. Martin and W.H. Finlay. Magnetic alignment of aerool particles for targeted pulmonary drug delivery: comparison of magnetic and aerodynamic torques. *Journal of Computational and Theoretical Nanoscience*, 2008a. Accepted.

A.R. Martin and W.H. Finlay. Alignment of magnetite-loaded high aspect ratio aerosol drug particles with magnetic fields. *Aerosol Science and Technology*, 42:295–298, 2008b.

S.H. Moolgavkar, R.C. Brown, and J. Turim. Biopersistence, fiber length, and cancer risk assessment for inhaled fibers. *Inhalation Toxicology*, 13:755–772, 2001.

A.D. Shine and R.C. Armstrong. The rotation of a suspended axisymmetric ellipsoid in a magnetic field. *Rheologica Acta*, 26:152–161, 1987.

W.C. Su and Y.S. Cheng. Deposition of fiber in the human nasal airway. *Aerosol Science and Technology*, 39:888–901, 2005.

Z. Ulanowski and P.H. Kaye. Magnetic anisotropy of asbestos fibers. *Journal of Applied Physics*, 85(8):4104–4109, 1999.

J.H. Vincent. *Aerosol Sampling: Science, Standards, Instrumentation, and Applications*. John Wiley and Sons, Ltd., 2007.

V.Timbrell. Deposition and retention of fibres in the human lung. *The Annals of Occupational Hygiene*, 26(1-4):347–369, 1982.

Q. Wang, B. Maze, H.V. Tafreshi, and B. Pourdeyhimi. Approaches for predicting colelction efficiency of fibrous filters. *Journal of Textile and Apparel Technology and Management*, 5(2), 2006.

N. Yamamoto, K. Kumagai, M. Fujii, D. G. Shendell, O. Endo, and Y. Yanagisawa. Size-dependent collection of micrometer-sized particles using nylon mesh. *Atmospheric Environment*, 39:3675–3685, 2005.

H.C. Yeh and B.Y.H. Liu. Aerosol filtration by fibrous filters - i. theoretical. *Aerosol Science*, 5:191–204, 1974.